



**Politecnico
di Torino**

Corso di Laurea Magistrale in Ingegneria
Aerospaziale

Tesi di Laurea Magistrale

**Computational Analysis of a Swirl
Distortion Generation Method Using the
Wishbone Vortex Generator.**

Supervisor:

Prof. Francesco Larocca

Mentor:

Prof. Nicolás García Rosa

Adrien Thacker

Simão Santos Rodrigues

Candidate:

Billal Es Saidi

This research was carried out at ISAE-Supaero's Department of Aerodynamics, Energetics and Propulsion (DAEP).

Acknowledgments

This research was conducted at the Department of Aerodynamics, Energetics and Propulsion (DAEP) at ISAE-Supaero.

I would like to thank my mentors at ISAE-Supaero, Prof. Nicolás García Rosa, Adrien Thacker and Simão Santos Rodrigues and my supervisor at Politecnico di Torino, Prof. Francesco Larocca for the support and inspiration they gave me.

I would also like to thank Nicolas Doué and Vincent Maillet for their help with the Star CCM+ software.

Finally, I would like to thank Julien Pedron for his support with the ISAE super-computer (Pando).

Abstract

Jet engines are used to intake air for their operation, unfortunately the air ingested always has a non-uniformity that affects engine operation and performance. While total pressure distortions have been widely studied, the influence of swirl distortions on engine performance is less well understood.

In order to analyse the interaction between swirl distortion and the engine, several methods have been created which are more or less accurate and complex. In this article a swirl distortion generation method, for a test bench, based on the use of vortex generators, more precisely of the Wishbone type, will be analysed computationally. The type of distortion of the vortex generator, the influence of the geometrical parameters on the generated distortion and the limits of this method will be defined.

In order to analyse the distortions generated by the Wishbone, a computational analysis of the target distortions generated by three different S-duct geometries was carried out. The three geometries differ from the geometric shape of the input section, and present three geometries that are close to those that are incorporated in new aircraft designs.

Contents

Acknowledgments	IV
Abstract	VI
1 Introduction	1
1.1 Total temperature distortion	2
1.2 Total pressure distortion	2
1.3 Swirl distortion	3
1.4 Distortion effect on engine	4
1.5 Objectives of present research	6
2 Literature Review	7
2.1 Serpentine Ducts	9
2.2 Methods for generating swirl distortion	12
2.2.1 Turned vanes	12
2.2.2 Delta wing	14
2.3 Swirl chamber	16
3 S-duct Computational Analysis	18
3.1 S-duct: Computational Setup	19
3.1.1 Air Intake with Circular Inlet	19
3.1.2 Air Intake with Semi-Circular Inlet	25
3.1.3 Air Intake with Rectangular Inlet	31
3.2 Inlet Duct Computational Results	35

3.2.1	Inlet-X Results	36
3.2.2	Inlet-Y Results	37
3.2.3	Inlet-Z Results	38
4	Wishbone Computational Analysis	41
4.1	Wishbone Vortex Generator: Computetional Setup	42
4.1.1	Wishbone Vortex Generator Geometry	42
4.1.2	Computational Domain	42
4.1.3	Mesh Generation	43
4.1.4	Phisics Models	46
4.1.5	Boundary Conditions	46
4.1.6	Simulation Results	47
5	Vortex Sensitivity to Geometric Parameters	50
5.1	Parametric Study Setup	50
5.2	Influence of the VG Width	51
5.3	Influence of the VG Chord	53
5.4	Influence of the VG height	56
6	Conclusions and Future Work	60
6.1	Research Outcome and Discussion	60
	Appendices	67
	Appendix A Potential Flow	67

List of Figures

1.1	Contours of total pressure for a typical total pressure distortion case.	3
1.2	Streamlines and contours of 2D velocity for a typical swirl distortion generated by a S-duct.	4
1.3	Effect of total pressure distortion on engine operability.[[14]]	5
2.1	Inlet system schematic from of the Tornado Fighter [16]	8
2.2	Flow conditioning with vortex generators.	8
2.3	Natural Vortices in a S-Duct. [31]	10
2.4	Switching and vertical modes (SM and VM respectively) at Mach number of 0.27. [11]	11
2.5	Turned vanes swirl distortion generators used by Genssler et al. [10].	12
2.6	Velocity fields created by turned vane type swirl generators created by Genssler et al. [10].	12
2.7	Swirl angle profile created by turned vane type twin swirl generator by Genssler et al. [10].	13
2.8	Parallel (red) and perpendicular (blue) lines plotted on top of a vector field from the serpentine inlet case [16].	14
2.9	Schematic of delta wing and assembly used by Genssler et al. [10] . .	15
2.10	Results obtained from a delta wing type swirl generator by Genssler et al. [10]	15
2.11	CAD model of typical swirl chamber for generation of bulk swirl. . . .	16
2.12	Possible swirl configurations that are obtainable using a swirl chamber as reported by Sheoran and Bouldin. [26]	17

3.1	Geometry of the S-duct Inlet-X.	21
3.2	Sketch of the S-duct Inlet-X Domain.	22
3.3	Mesh scene of the entrance section of Inlet-X.	23
3.4	RMS residuals for Inlet-X simulation.	26
3.5	Geometry of the S-duct Inlet-Y.	26
3.6	Geometry of the S-duct Inlet-Y.	28
3.7	Mesh scene of the entrance section of Inlet-Y.	28
3.8	Turbulent Flat Plate Boundary Layer Profiles.	30
3.9	RMS residuals for Inlet-Y simulation.	30
3.10	Geometry of the S-duct Inlet-Z.	31
3.11	Sketch of the S-duct Inlet-Z Domain.	32
3.12	Mesh scene of the entrance section of Inlet-Z.	33
3.13	RMS residuals for Inlet-z simulation.	34
3.14	Swirl angle definition. [16]	35
3.15	Inlet-X: Symmetry Plane Total Pressure Recovery Profile.	36
3.16	Inlet-X: swirl angle profile (a) and streamlines in the AIP (b).	37
3.17	Inlet-Y: Symmetry Plane Total Pressure Recovery Profile.	37
3.18	Inlet-Y: swirl angle profile (a) and streamlines in the AIP (b).	38
3.19	Inlet-Z: Symmetry Plane Total Pressure Recovery Profile.	39
3.20	Inlet-Z: swirl angle profile (a) and streamlines in the AIP (b).	40
4.1	Wishbone Geometry. [38]	42
4.2	Wishbon domain.	43
4.3	Mesh scene in the symmetry plane and in the AIP.	44
4.4	Mesh convergence.	47
4.5	Inlet-Y: swirl angle profile (a) and streamlines in the AIP (b).	48
4.6	Representation of the evolution of streamlines, arriving from the inlet, interacting with the Wishbone.	49
5.1	Position of the vortex core as a function of s^*	52
5.2	R_0 contour in the symmetry plane.	53
5.3	Swirl angle contour.	54

5.4	Maximum axial vorticity as a function of the parameter s^*	55
5.5	Position of the vortex core as a function of c^*	55
5.6	R_0 contour in the symmetry plane.	56
5.7	Swirl angle contour.	57
5.8	Maximum axial vorticity as a function of the parameter c^*	58
5.9	Position of the vortex core as a function of h^*	58
5.10	Swirl angle contour.	59
A.1	Inlet-Y: swirl angle profile (a) and streamlines in the AIP (b).	68

List of Tables

3.1	Inlet-X geometry parameters.	21
3.2	Inlet-X overall geometry parameters.	23
3.3	Inlet-X: mesh features.	24
3.4	Inlet-X Boundary Conditions.	25
3.5	Inlet-Y overall geometry parameters.	27
3.6	Inlet-Y: mesh features.	29
3.7	Inlet-Z overall geometry parameters.	32
3.8	Inlet-Z: mesh features	33
3.9	Inlet-Z Boundary Conditions.	34
4.1	Overall Wishbone geometry parameters.	43
4.2	Mesh features.	45
4.3	Physics Models for Wishbone Simulations.	47
4.4	Wishbone Domain Boundary Conditions.	48
5.1	Definition of parameter variation ranges.	51

Chapter 1

Introduction

Recent research programs show interest in a configuration of modern conceptual aircraft designs that shift the position of the engine from the conventional wing-supported pylon to near or full integration with the airframes. The choice of this new approach stems from the increasingly restrictive regulations on environmental and noise pollution. In fact, this new aircraft concept tends to improve performance, both from an aircraft and engine point of view. The integration of the engine inside the aircraft leads to the ingestion of the boundary layer and this has two main advantages:

- The first advantage is the reduction of momentum deficits downstream of the aircraft, reducing the drag of the aircraft.
- The second advantage is related to the propulsive efficiency, expressed as:

$$\frac{\textit{Work done on the aircraft}}{\textit{Energy imparted to the engine air flow}} \quad (1.1)$$

If we consider the mass flow of the fuel to be negligible compared to the air flow, the thrust can be simplified with the following equation:

$$F = \dot{m}(v_j - V) \quad (1.2)$$

where \dot{m} is the mass flow rate of the combustion gases, v_j is the velocity of

the combustion gases at the exit of the engine and V is the flight velocity. Looking at the formula it becomes apparent that by reducing the flight speed, for example by ingesting the boundary layer, the thrust is increased for the same flow rate and speed of exhaust gases. So this would allow a reduction in fuel consumption.

Despite all these advantages of this architecture coupling the engine to the airframe, it causes inlet flow distortions, in other words it leads to non-uniform inlet conditions. The distortions can be of three types, and in some cases they can all be present at the same time. These distortions cause the engine to operate off-design even when in on-design conditions, degrading the operating performance.

- Total pressure distortion.
- Total temperature distortion.
- Swirl distortion

1.1 Total temperature distortion

The total temperature distortion is related to the non-uniformity of the total temperature at the turbomachine inlet. While it is easy to imagine a non-uniformity of total temperature at the inlet of the high-pressure turbine, which is located immediately after the combustion chamber, it is difficult to imagine what could cause a distortion of total temperature at the inlet of the engine. Typically this distortion is caused by the ingestion of hot gases generated by armament firing, recirculation of exhaust gases as in the STOL-VTOL (Vertical or Short Take-Off and Landing) case or the ingestion of exhaust gases from other aircraft.

1.2 Total pressure distortion

Total pressure distortion compared to total temperature distortion is more common, and is caused by several factors such as boundary layer ingestion, extreme manoeuvring or by complex air intakes typical of embedded engines. A typical example of

total pressure distortion is shown in Figure 1.1. The Figure 1.1 is the result of a RANS simulation of a flow inside an S-Duct.

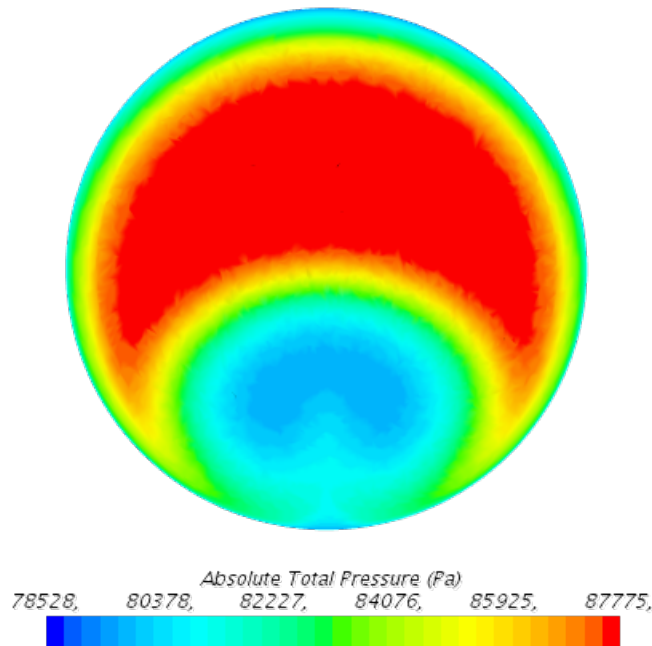


Figure 1.1: Contours of total pressure for a typical total pressure distortion case.

Total pressure distortion has always been of high interest because its presence is neither insignificant nor rare. For this reason, many research works have tried to understand the response of the engine to this type of distortion. Nowadays in the literature there are many researches that have led to the creation of screens that allow to recreate different types of total pressure distortions that do not represent perfectly the reality but allow to better understand the response of the engine to this non-uniformity for ground tests [7, 25].

1.3 Swirl distortion

Swirl distortion is linked to the presence of non-uniform velocity components in the cross plane. Also in this case, the non-uniformity can be caused by the ingestion of the boundary layer, by more or less complex air intakes or by vortices generated on the ground or by other upstream aircraft components. An example of this type of distortion is shown in Figure 1.2, in which the streamlines in the plane at one exit

radius downstream from the S-duct exit are shown, the module of which is depicted through the contours.

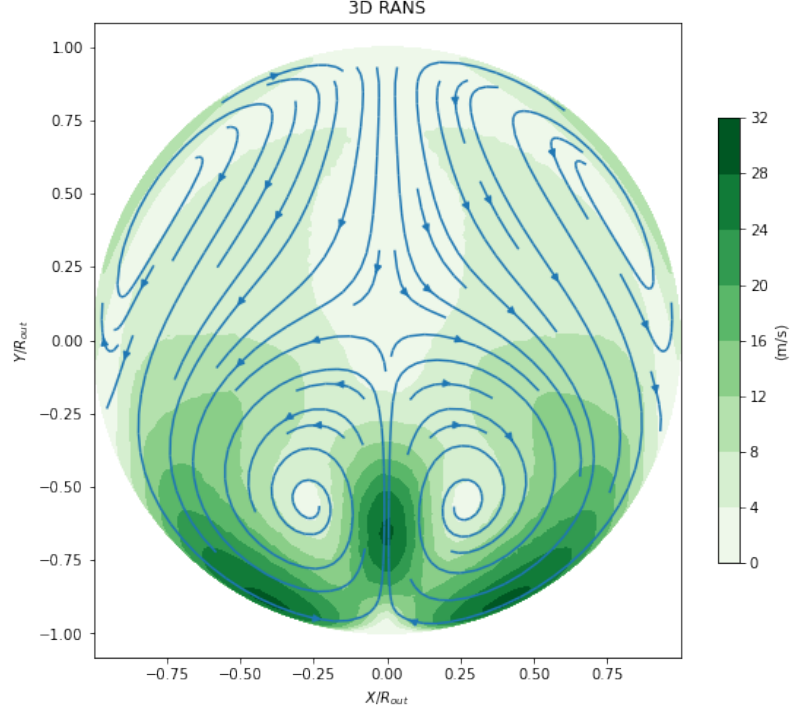


Figure 1.2: Streamlines and contours of 2D velocity for a typical swirl distortion generated by a S-duct.

Due to the relatively complicated nature of the swirl distortion, as well as difficulties in its recreation, it has not been studied as intensively as total pressure distortion. However, new airframe designs inspired by the constant search for higher performance have caused the jet engine testing community to start placing greater importance on evaluating the effects of swirl distortion [4, 29]. Early methods of swirl generation were aimed at testing a generic, low-fidelity profile. For this reason there were many cases where inconsistencies between ground and flight tests emerged [30].

1.4 Distortion effect on engine

During the design of turbomachines, the blades are designed to work with maximum performance at operating points that correspond to specific input conditions. Usually, the operating point chosen for the design of the turbomachine is the cruise, as the engine works in this phase for most of the flight. The design conditions usu-

ally coincide with the point of maximum efficiency. It can be understood that with non-uniform conditions at the engine input the blades pass through distortion zones and therefore work under non-optimal conditions. This reduces the performance and operability of the engine [8, 21, 24, 28]. In fact, as shown in Figure 1.3, the presence of distortions at the engine input also affects the surge margin. Figure 1.3 shows the results of a study done by Hercock and Williams to test the effect of total pressure distortion on engine operability [14]. In their study, the authors subjected an engine to several different patterns of total pressure distortion.

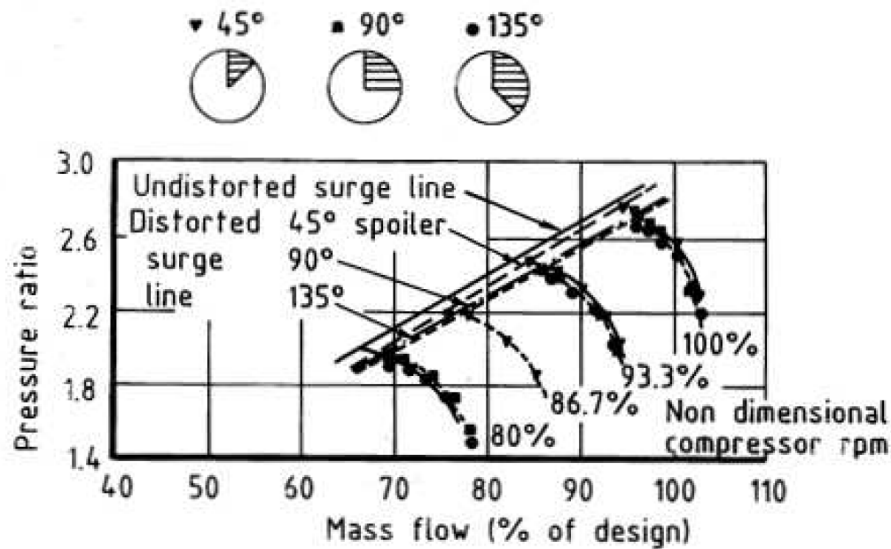


Figure 1.3: Effect of total pressure distortion on engine operability.[[14]]

In addition, several studies have concluded that swirl distortion also has an effect on the operability of the engine. The presence of distortion as seen in Figures 1.1 and 1.2 forces the load on the blade to change periodically. The unsteady load on the blade results in fatigue wear of the blade [13, 19]. Therefore, the presence of distortion not only affects the performance of the engine but also the maintenance cycles, which obviously increases costs. It is therefore clear that a numerical and experimental study of the compatibility of the airframe engine is indispensable before flight tests.

1.5 Objectives of present research

Given the inevitable presence of these distortions, it is essential to understand how the engine behaves in their presence. This is usually done by numerical and experimental simulations, which in turn are divided into ground and flight tests. Flight tests are more expensive than ground tests, so there is a tendency to have ground tests that are as reliable as possible in order to reduce the number of flight tests. Therefore, in the following work, a swirl distortion generation method for ground tests is proposed. This method is based on the use of vortex generators, specifically the Wishbone vortex generator. Through numerical simulations conducted using Star CCM+, an investigation of this vortex generation method will be carried out.

Chapter 2

Literature Review

While the generation of total pressure distortions is nowadays a fairly well-known field, the same cannot be said for the generation of swirl distortions. In fact, total pressure distortions have been extensively studied since the 1950s [22, 9], leading to the creation of wire mesh screens that have been increasingly optimised over the years. The investigation of swirl distortions has been relatively limited compared to total pressure distortions. Research on swirl distortion generators began in the late 1980s [10]. During these years, in fact, anomalies appeared during flight tests of the Tornado fighter that did not appear during ground tests. The Tornado fighter has two turbofans integrated into the fuselage, and powered by a serpentine duct. The geometry of the propulsion system is shown in Figure 2.1. The anomalies found during the first flight test are related to the presence of swirl that caused one of the two engines to surge when the aircraft was being flown at high angle of attack and the other engine to surge when the aircraft was flown at high Mach number.

A first solution adopted to reduce the effects of swirl distortion is the active or passive use of guide vanes or vortex generators inside the air intake as shown in Figure 2.2 [38, 32, 18, 17].

The main task of the guide vanes is to energise the boundary layer in order to delay the separation inside the intake as much as possible, thus reducing the swirl distortion and the total pressure distortion. The presence of the guide vanes was very

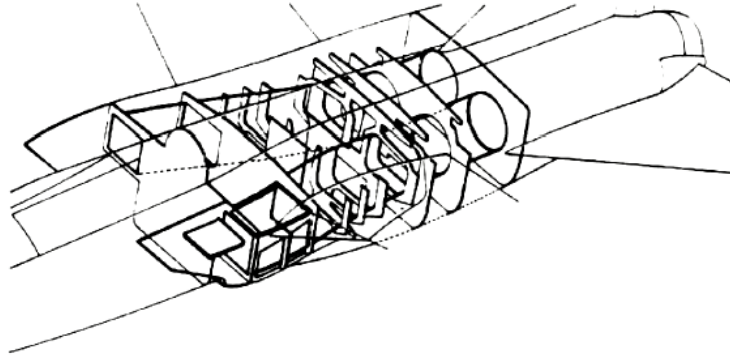
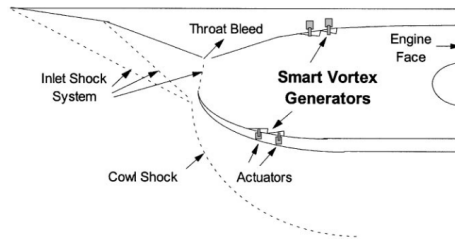
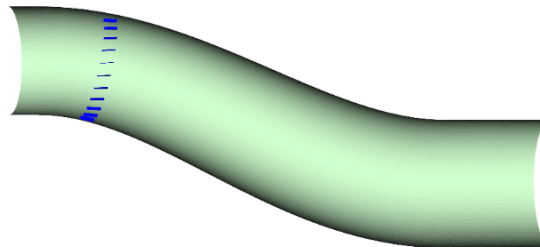


Figure 2.1: Inlet system schematic from of the Tornado Fighter [16]



(a) A schematic drawing of smart (subsonic) vortex generators in a supersonic inlet [6].



(b) Vortex generator installation in the RAE M2129 S-duct [17].

Figure 2.2: Flow conditioning with vortex generators.

beneficial and also allowed to reduce the length of the air intakes thus reducing ram drag and engine weight which results in reduced fuel consumption [17]. Another method of reducing vortex distortions generated by air intakes in engines integrated in the fuselage is to use actively controlled Whishbone or Delta type vortex generators to adapt to various flight configurations [6]. Nowadays, research is focusing on optimising the geometry of the S-duct to avoid introducing objects with non-negligible drag into the intake [5]. Therefore, the Tornado fighter can be considered the first aircraft to introduce investigations into the effects of swirl distortion on

compressor performance and operability. It was then necessary to start creating devices that could recreate the swirl distortions in the test bench.

2.1 Serpentine Ducts

The use of S-ducts has shown many advantages in terms of operating costs, fuel efficiency and noise levels produced by the engine. Due to the centerline offset, which characterises this duct, in diffusing ducts the airflow can be slowed down and compressed faster than conventional straight ducts, allowing a shorter design that saves weight. It has been estimated by Chen and Wang [2] that the net weight of an aircraft could be reduced by 15% if the fuselage length was reduced by an inlet diameter. Despite these advantages, the S-duct causes non-uniformity of flow at the engine inlet, which degrades engine performance and limits its operability. The problems associated with the S-duct have led motorists since the 1950s to study the phenomena which occur inside the S-duct. A numerical investigation by Kramer and Stanitz [20] sought to better describe the behaviour of real fluids in a fluid machinery environment. They investigated two dimensional, incompressible, inviscid shear flows in a 90 degrees elbow. With an increase in negative vorticity, the static pressure drop through the elbow; however, there was only a slight change in the local pressure coefficient which was relatively similar for corresponding positions on either wall. The pressure drop along the inside of the turn was well represented as was the corresponding increase in velocity. Rowe (1970) [23] reported on flow in 180° bends and a 45°/45° S-duct and compared the experimental measurements with inviscid theory. Rowe described the counter-rotating vortices formed in turning ducts. The ducts he investigated were all of circular cross section and therefore produced vortices at the centre of the inside turn. In the 180° bend studied, Rowe found that over 61 pipe diameters were required for the flow to return to the pre-turn flow uniformity following the end of the bend. In the S-duct tested by Rowe, the same radius of curvature and duct cross sectional geometry as the 180 degree bend were used, but only about 13 pipe diameters were required for the flow to return to the pre-turn flow uniformity. This implies that the second turn of the S-duct tends to dissipate

the effect of the first turn. In addition, in the S-duct, the flow is turned only 45 degrees at a time. In a separate study, by Sullivan et al. (1982) [31], the S-duct under investigation involved two 45 degree turns. In this case flow separating vortex pairs were produced at the bottom (inside) of the first turn and the top (inside) of the second turn. This process was documented through dye injection in a water tunnel, and the results show the importance of the severity of the turn in producing secondary flow fields. A schematic of the vortex development captured through photographs is shown in Figure 2.3. Here the two sets of counter-rotating vortices formed at each turn can be seen clearly.

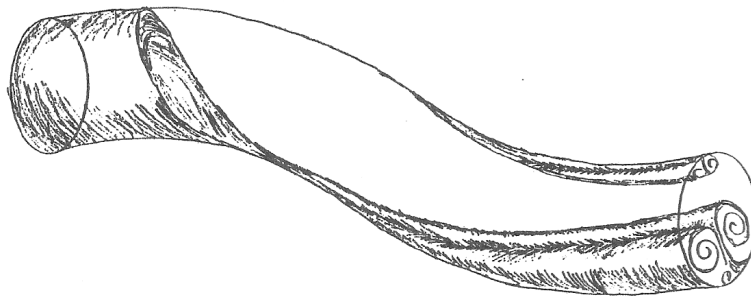


Figure 2.3: Natural Vortices in a S-Duct. [31]

Thanks to the development of computational power and progress in the experimental field, it has been possible to characterise the flow in an S-duct more and more. Depending on the diffusion rate, the radius of curvature of the two elbows, and the intensity of the secondary flows, the flow is expected to separate near the [36, 34] inflection point. The radius of curvature generates a radial pressure gradient which, together with the compression rate, generates secondary flows that make the flow purely 3D. In the first elbow the pressure increases in the outer wall, contrary to the inner wall increasing the boundary layer thickness without causing separation [1, 35]. while in the second elbow the deceleration in the outer wall together with the compression rate causes separation. Separation which is the main cause of total pressure losses along with secondary flows. In the AIP the total pressure loss is located in the lower central part and in two small areas in the upper part of the section [33, 40, 35]. From the solutions found in the literature it can be stated

that the time-averaged solution has two large symmetrical counter-rotating vortices [36, 35]. The two counter-rotating vortices are formed after the second elbow [12]. As demonstrated by Wellborn these two counter-rotating vortices are generated due to secondary flows that drags the flow from the boundary layer to the duct core degrading the uniformity of the pressure profile. In spite of these considerations made on stationary calculations, averaged over time, the unsteady phenomenon is asymmetrical [39]. This unsteadiness is caused by separation and is characterised by two large vortices. Measurements of the unsteady flow were conducted by Gil-Prieto et al. [11] in two circular S-shaped ducts at Mach 0.27 and 0.6. In their analysis, two ducts with different height-to-length ratios were analysed. The unsteadiness was quantified by a sample of statistically representative data. The results showed that the time-averaged solution has different characteristics to the unsteady solution. It can be seen that although the pressure recovery deviation can be neglected, the swirl deviation can be of an order of magnitude. Gil-Preto et al.[11] also conducted an analysis of the PIV (Particle Image Velocimetry) strereoscope data with which they showed the switching and vertical mode characterising the flow (Figure 2.4).

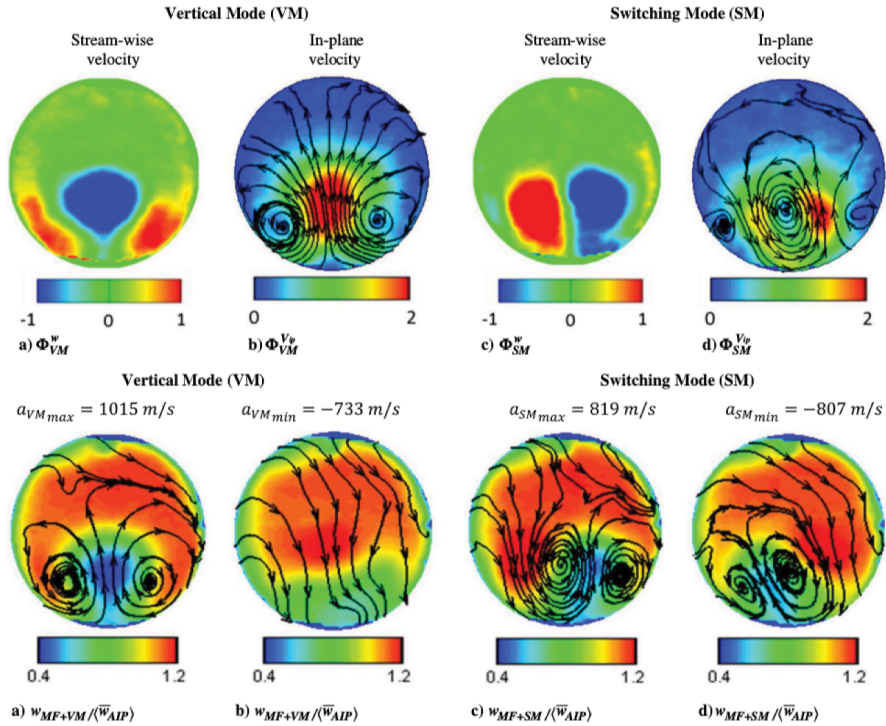


Figure 2.4: Switching and vertical modes (SM and VM respectively) at Mach number of 0.27. [11]

2.2 Methods for generating swirl distortion

2.2.1 Turned vanes

Turned vanes are similar to the guide vanes used to reduce swirl distortion in different jet engines. Two examples of Turned vanes studied by Genssler et al. are shown in Figure 2.5 [10]. These two Turned vanes are not designed to recreate any vortex configuration generated by an airframe/engine combination, but are intended to create generic vortex structures that are similar to those found in reality.

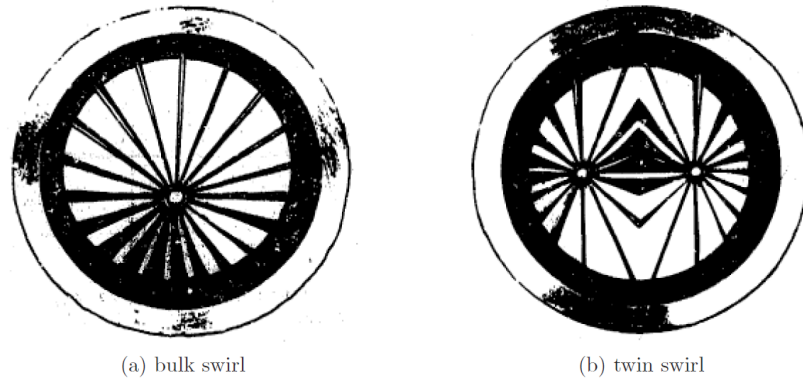


Figure 2.5: Turned vanes swirl distortion generators used by Genssler et al. [10].

Figure 2.5(a) shows the Turned vanes for bulk swirl generation while Figure 2.5(b) shows those for twin swirl generation. The velocity field related to the turned vanes used by Genssler et al. is shown in Figure 2.6.

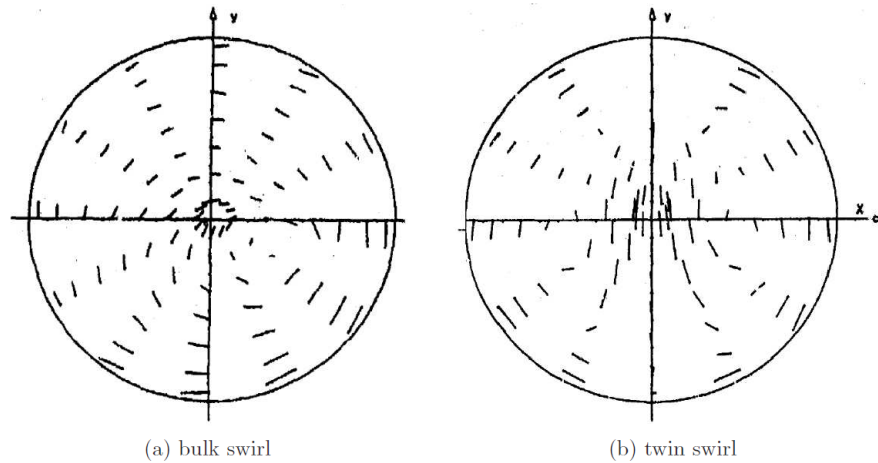


Figure 2.6: Velocity fields created by turned vane type swirl generators created by Genssler et al. [10].

It can be seen that qualitatively the author was able to produce the two types of swirl. In order to make a quantitative comparison as well the swirl angle profile along the x-axis was plotted, Figure 2.7.

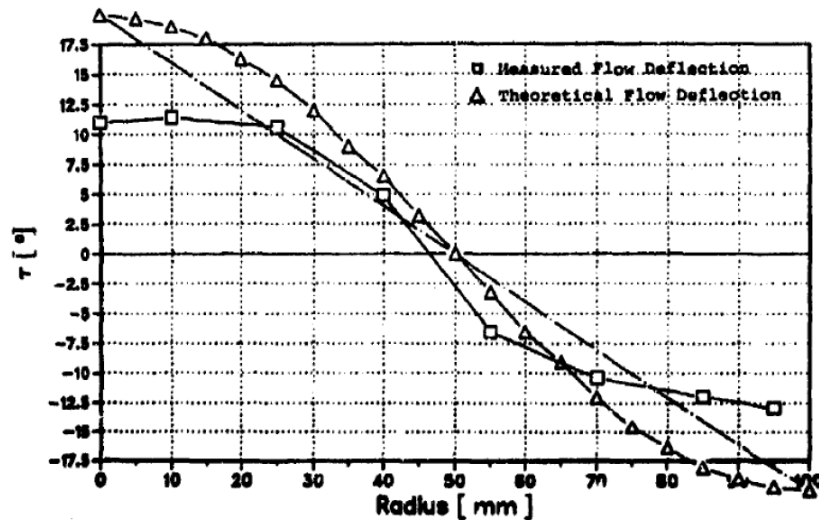


Figure 2.7: Swirl angle profile created by turned vane type twin swirl generator by Genssler et al. [10].

It can be seen that the two curves have almost the same trend, but despite this the two curves could not be matched. The authors justify this deviation to the technological limitation found in the generation of the Turned vanes. This limitation is mainly due to the use of straight vanes instead of curved vanes which, according to the authors, would have been more efficient in reproducing the two types of swirl. This configuration of curved and not straight vanes was developed by Hoopes and al.[16]. In this case the vane lines, Figure 2.8 are defined perpendicular to the velocity field which was being tried to reproduce. The vane lines are placed on a seed line as being in the form of a linear cascade. Once the vane lines have been created, the geometry of the cross sections along each vane line must be determined. At regular intervals along each vane line, the original vector field is queried to find the desired turning angle at the given position. Once the desired turning angle is known, it is used along with other parameters, such as the distance to the nearest two vanes and the desired vane thickness and solidity, to calculate the needed vane cross section.

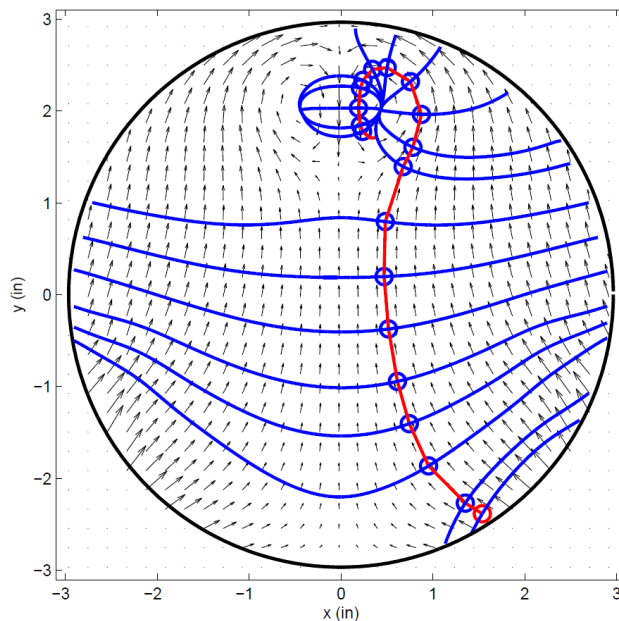


Figure 2.8: Parallel (red) and perpendicular (blue) lines plotted on top of a vector field from the serpentine inlet case [16].

2.2.2 Delta wing

Another method, studied by Genssler et al., is the delta-wing method. Until 1983, knowledge of the structure of the vortices generated by a delta wing was still based on experimental results. This forced his design to be purely empirical. It was not until 1983 that Hoejimakers et al. [15] succeeded in modelling the structure of the vortexes generated by the delta wing and thus also developed calculation methods for the detailed determination of the structure of the wake flow field. As is known at that time, the delta wing at a certain incidence produces a pair of counter-rotating vortexes, the intensity of which depends on the angle of incidence. In order to study the behaviour of the vortexes generated by the wing, Genssler et al. created a mechanism to keep the wing fixed and to change its attitude through a series of actuators. Figure 2.5 shows the mechanism used and the delta wing.

The wake is measured through a set of three 5-hole pressure probes. The results obtained are shown in Figure 2.6 [16]. Figure 2.6 a shows a plot of the velocity vector while figure 2.6b shows the development of the swirl angle as a function of the theta angle. The curves shown in Figure 2.6b represent the same phenomenon but with

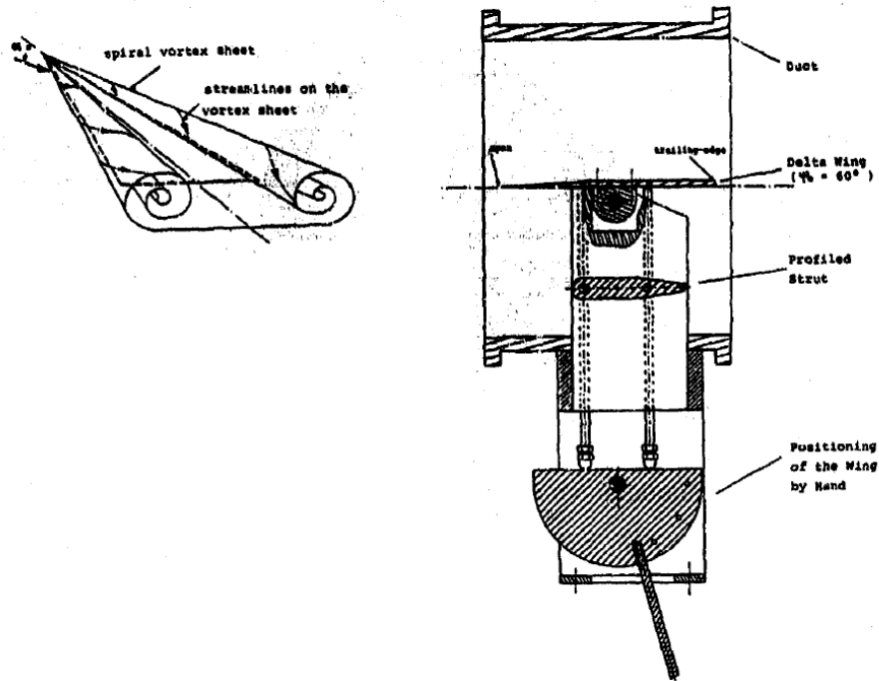


Figure 2.9: Schematic of delta wing and assembly used by Genssler et al. [10]

different figure tools and we also show the cosine distribution that represents the ideal trend for two counter-rotating vortices.

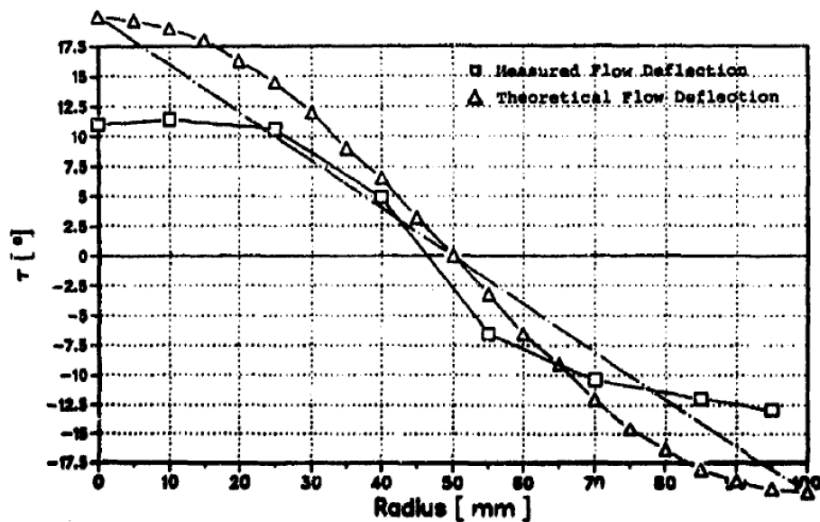


Figure 2.10: Results obtained from a delta wing type swirl generator by Genssler et al. [10]

It can be seen that there is a better match of the ideal solution by the vortexes generated by the delta wing than that generated by the method Turned vanes. In addition, the delta wing is also a very simple object to create, which is a very positive

point. Unfortunately, with the delta wing you can only generate one type of vortex and therefore it is often complicated to reproduce the reality.

2.3 Swirl chamber

A further method of generating swirl distortions that has recently appeared is the swirl chamber. The swirl chamber consists of a plenum with one or more inlet doors and an outlet pipe as shown in Figure 2.11.

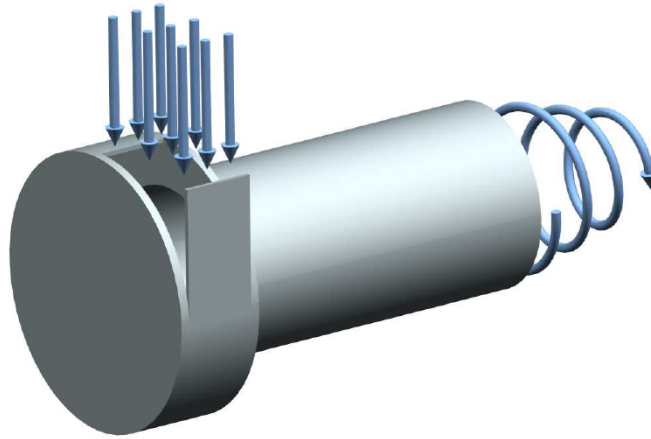


Figure 2.11: CAD model of typical swirl chamber for generation of bulk swirl.

This method of generating swirl distortion has been extensively studied. Sheoran and Bouldin have conducted several analyses of the swirl chamber behaviour [26, 27]. The authors focused on studying different chamber configurations to obtain different swirl patterns at the chamber exit as shown in Figure 2.12.

This method of generating swirl distortion has the advantages of being able to regenerate different swirl patterns and does not isolate objects in front of the motor which can be ingested. However, the swirl distortions recreated by the swirl chamber are generic and therefore the particular swirl profile cannot be recreated.

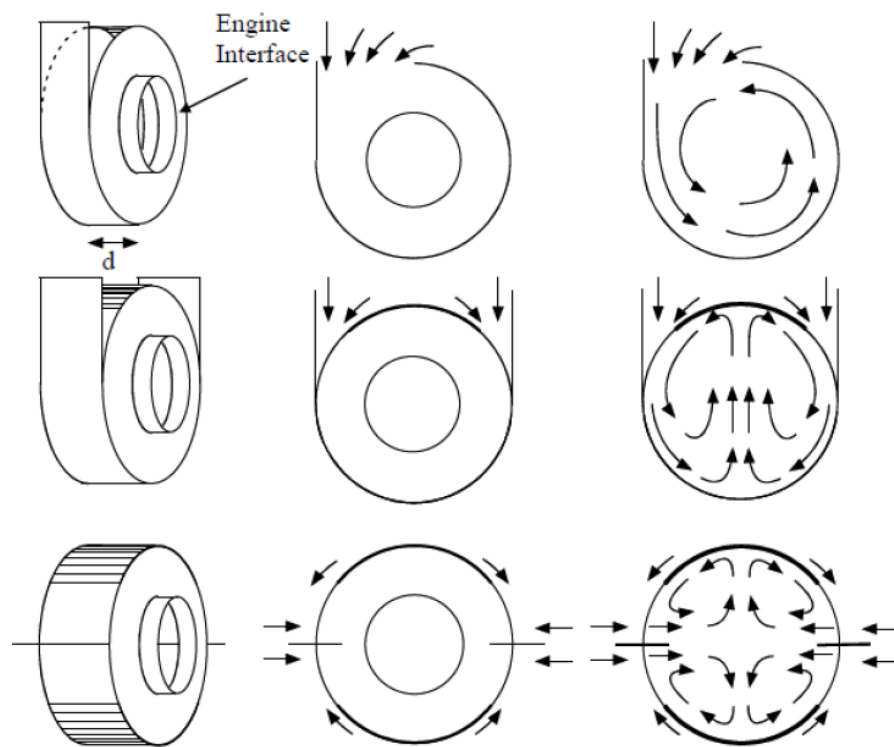


Figure 2.12: Possible swirl configurations that are obtainable using a swirl chamber as reported by Sheoran and Bouldin. [26]

Chapter 3

S-duct Computational Analysis

Before presenting the swirl distortion generation method, a target distortion profile must be defined. This can be defined in 3 different ways:

- Analytical.
- Through CFD.
- Experimental.

Analytical means defining the distortion by mathematical equations that model e.g. vortexes. Since this approach is only a simplified approximation of the reality, in some cases it is difficult to interpolate the reality. In addition, the analytical definition of distortion can also lead to nonphysical solutions since physical and geometric variables can be changed without restriction. The CFD (Computational Fluid Dynamic) definition of distortion is more accurate and less flexible than the analytical one. Nevertheless, it is still possible to change the geometric variables and the physical characteristics of the fluid dynamic, which again leads to inconsistencies. The definition of distortion from experimental results or from flight or ground tests is a very reliable solution but at the same time not flexible.

In the present work it was decided to follow the computational approach. The swirl distortion pattern was obtained by simulating three different S-duct geometries. The geometries considered are readily available in the literature [9, 5, 3]. The main

difference between these three geometries is the shape of the air intake inlet. For convenience, these geometries will be denominated Inlet-X, Inlet-Y and Inlet-Z for air intakes with circular, semi-circular and rectangular inlets respectively. These types of ducts, although not designed to be integrated into aircraft in operation, may be representative for the new generation of intakes installed in aircrafts with integrated airframe/engine architectures in terms of distortions and characteristics [9, 3, 5, 11]. For simplicity, the presence of a fan at the exit of the duct was not taken into account. The duct geometries were scaled to respect the dimensions of the fan used for the experimental simulations in the ISAE-Supaero research laboratory. The computational analysis was carried out with flow conditions that allow for the same swirl conditions at the AIP as those obtained by D'Ambrosio et al.[5], Frohnäpfel et al.[9] and Chiang et al.[3] in their analysis. This was achieved by imposing the same correct flow rate between the scaled geometry and the reference geometry.

Therefore, in this chapter the procedure through which the target distortion profiles was obtained is described. Furthermore the geometry of the S-ducts will be described as well as the imposed physical conditions. To conclude an analysis of the effects of the boundary layer and the S-duct on the flow in the section of interest (AIP).

3.1 S-duct: Computational Setup

3.1.1 Air Intake with Circular Inlet

Geometry

The first S-duct model, shown schematically in Figure 3.1, selected for the generation of one of the target distortions is an S-duct with circular inlet and outlet. This type of S-duct was designed by Wellborn [36, 5] to study the behaviour of a compressible flow inside this duct, through both numerical and experimental analysis. It was then used by D'Ambrosio to conduct an optimisation of the duct to reduce distortion levels at the AIP. For simplicity in this work it will be called Inlet-X.

The duct centerline is defined by two planar circular arcs with same radii, R , and subtended angles, $\theta_{max}/2$. Its coordinates are defined by the following equations:
For $0 \leq \theta \leq \theta_{max}/2$:

$$x_{cl} = R \sin \theta \quad (3.1)$$

$$z_{cl} = R \cos \theta - R \quad (3.2)$$

$$y_{cl} = 0 \quad (3.3)$$

For $0 \leq \theta \leq \theta_{max}2$:

$$x_{cl} = 2R \sin \theta - R \sin \theta_{max} - \theta \quad (3.4)$$

$$y_{cl} = 2R \cos \theta - R - R \cos \theta_{max} - \theta \quad (3.5)$$

$$z_{cl} = 0 \quad (3.6)$$

The duct sections perpendicular to the centerline are circumferences of radius defined by the following equation:

$$\frac{r}{r_i} = 1 + 3 \left(\frac{r_e}{r_i} - 1 \right) \left(\frac{\theta}{\theta_{max}} \right)^2 - 2 \left(\frac{r_e}{r_i} - 1 \right) \left(\frac{\theta}{\theta_{max}} \right)^3 \quad (3.7)$$

where r_i is the entrance radius and r_e is the exit radius.

This duct presents an area expansion ratio (A_e/A_i) of about 1.56. This expansion ratio is guaranteed by a length of about four outlet diameters (L), and by an offset of about one outlet diameter (ΔH). For the generation of the distortion it was necessary to scale the geometry of the Wellborns S-duct in order to have the outlet diameter equal to the diameter of the duct where the Wishbone vortex generator will be placed, and therefore the diameter of the fan present in the ISAE-Supaero research laboratory. The geometrical parameters of the scaled geometry are shown in Table 3.1.

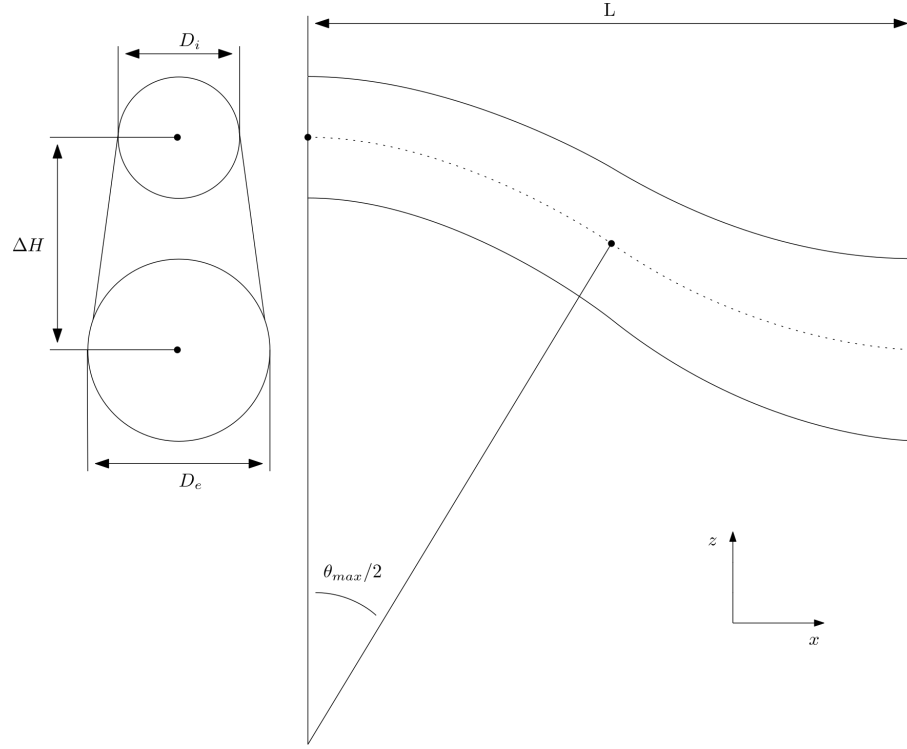


Figure 3.1: Geometry of the S-duct Inlet-X.

Table 3.1: Inlet-X geometry parameters.

Parameter	Value
$\theta_{max} (^{\circ})$	60
$R (m)$	1,43
$r_i (m)$	0,141
$r_e (m)$	0,176

Computational Domain

Before defining the computational domain, it is necessary to define the Aerodynamic Interface Plane (AIP) that allows to justify the geometrical shape of the computational domain. The AIP is generally an arbitrarily defined plane used by airframe/engine designers to identify the flow transition from the outlet of the air intake to the inlet of the fan. In the present research it was decided to place the AIP after the S-duct exit at a distance equal to the duct exit radius. This distance

allows the flow reattachment stabilising the distortion, but still this distance allows the distortion to be maintained at significant levels for testing purpose.

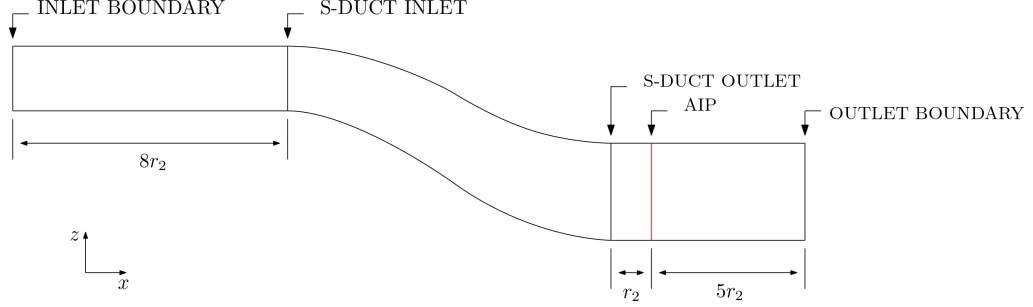


Figure 3.2: Sketch of the S-duct Inlet-X Domain.

The computational domain chosen is the same as that used by D'Ambros, in order to reproduce the same swirl distortion at AIP. The domain consists of three ducts: the inlet duct, the S-duct and the outlet duct. The inlet duct is a straight duct with a length of 8 radii, and guides the airflow towards the S-duct. Immediately after the inlet duct we find the S-duct whose characteristics have been discussed previously. The outlet duct is located immediately after the S-duct and has a length of 6 exit radii. The outlet duct contains the AIP, which is located one outlet radius from the S-duct outlet for the reason explained above. The length of the outlet duct is important to ensure that there are no interactions between the outlet boundary conditions and the solution in the AIP. The Table 3.2 shows the geometric parameters of the calculation domain, together with the parameters that most characterise the S-duct.

Mesh Generation

The Polyhedral Mesher was chosen for mesh generation, which creates an unstructured mesh with polyhedral-shaped cells Figure 3.3. In addition in Figure 3.3 it is possible to see prismatic cell layers next to the wall which allows the boundary layer to be captured accurately.

The thickness of the first layer was chosen to ensure a y^+ less than 1 throughout the duct. The total thickness of the prism layer was chosen to contain the boundary layer. The main characteristics of the mesh are summarised in Table 3.3.

Table 3.2: Inlet-X overall geometry parameters.

Geometric Parameter	Reference Variable	Value
S-duct Length (m)	L	1,084
Centerline Offset (m)	ΔH	0.3566
Outlet Duct Length	L_{out}	3,080
AIP Position	L_{AIP}	1,039
Length-to-Diameter Ratio	L/D_e	1,069
Centerline Shift Ratio	$\Delta H/D_e$	1,069
Area Ratio	A_e/A_i	1,069

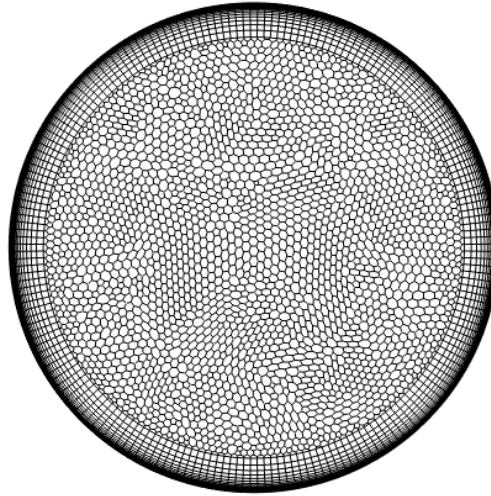


Figure 3.3: Mesh scene of the entrance section of Inlet-X. .

Physics models

The fluid, considered for the numerical simulation, is air modelled as an ideal gas in order to consider the effects of compressibility. For simplicity and in order not to make the simulations computationally onerous, it was decided to conduct stationary simulations which therefore provide a steady solution. This does not allow us to take into account the unsteadiness discussed in the literature review, which can be

Table 3.3: Inlet-X: mesh features.

Method	Unstructured Polyhedral Mesher
Target Surface Size (m)	0.005
Surface Growth Rate	1.1
Number of Prism Layers	35
Prism Layer Stretching	1, 25
Prism Layer Total Thickness	0.0197
Cells	6389568
Verts	19180716

neglected for the type of study we want to do in this paper. For solving the conservation equations for mass, momentum and energy, coupled flow models with the coupled energy extension were chosen. These models are robust to solve compressible flows and doesn't deteriorate the convergence rate as the mesh is refined. For simplicity no boundary layer transition model was adopted but a turbulent boundary layer was imposed, this is justified by the high Reynolds number ($\sim 3.8 \cdot 10^6$) at the duct inlet. The $k-\omega$ turbulence model was used due to the separations that are established in the lower part of the S-duct. In fact, this model, besides being less dissipative than, for example, the $k-\epsilon$, is able to better predict the position of a separated flow. The physical models described here will be the same for all three geometries, which is why they are only shown in this section.

Boundary Conditions

The boundary conditions chosen for the simulation are those used by d'Ambros to match the experimental conditions described in [5]. For the boundary conditions on Star CCM+, we imposed the inlet as Stagnation Inlet, and the outlet as Pressure Outlet, so for the boundary conditions we only need the total and static pressure at the inlet while for the outlet we need the static pressure and the static temperature.

The boundary conditions are collected in Table 3.4.

Table 3.4: Inlet-X Boundary Conditions.

Parameter	Value
Inlet total pressure (Pa)	88744
Inlet static pressure (Pa)	69575
Outlet static pressure (Pa)	78982
Total temperature (K)	286,3

Convergence Criteria

It was considered necessary to have the RMS residual for the continuity, momentum, and energy equations below 10^{-3} as a convergence criterion. As shown in Figure 3.4, 10000 iterations are sufficient to satisfy this criterion. So it was decided to stop at 10000 iterations even though the residuals seem to keep decreasing. Furthermore, in the residuals plot, the residuals of the Turbulent Kinetic Energy (TKE) and Specific Dissipation Rate (SDR) equations are also presented. The residuals of the latter two equations also satisfy the criterion by going below 10^{-4} .

3.1.2 Air Intake with Semi-Circular Inlet

Geometry

The second model of S-duct chosen for the simulation is the Inlet-A developed by NASA for experimental research purposes on the effects of distortions on a fan [37]. This type of duct, although not designed to be integrated into aircraft in operation, may be representative for some of the intakes installed in the new generation of aircraft with integrated airframe/engine architectures, in terms of distortions and characteristics. In order to make this simulation as representative as possible of reality, boundary layer ingestion will be imposed at the entrance of the S-duct. In the present work, the scaled Inlet-A is called Inlet-Y.

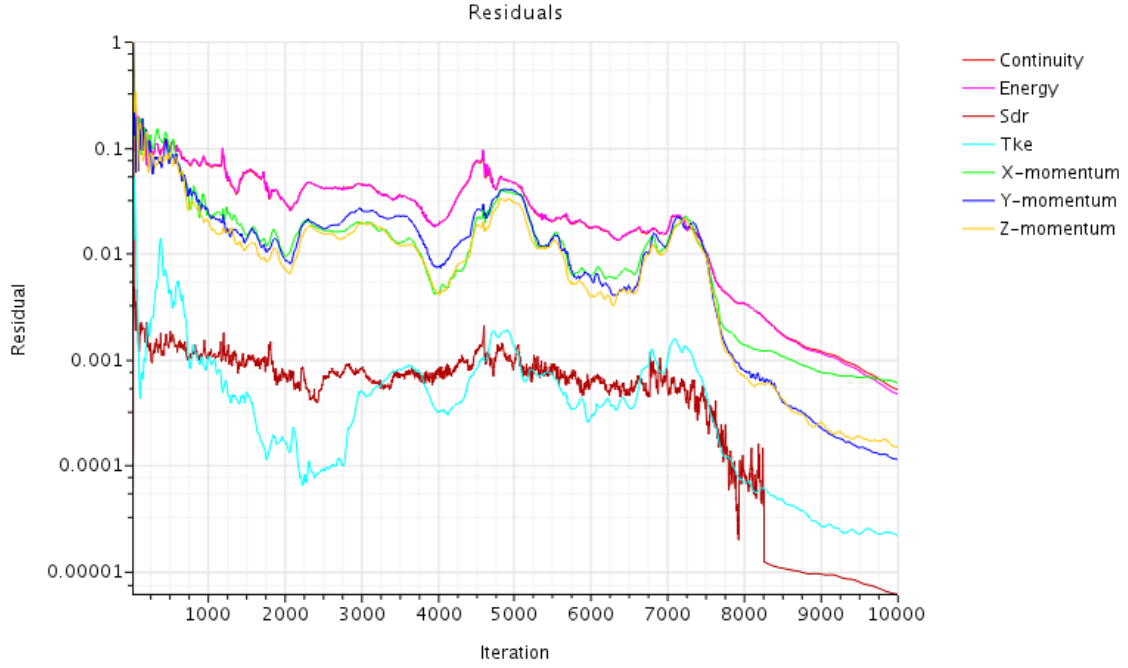


Figure 3.4: RMS residuals for Inlet-X simulation..

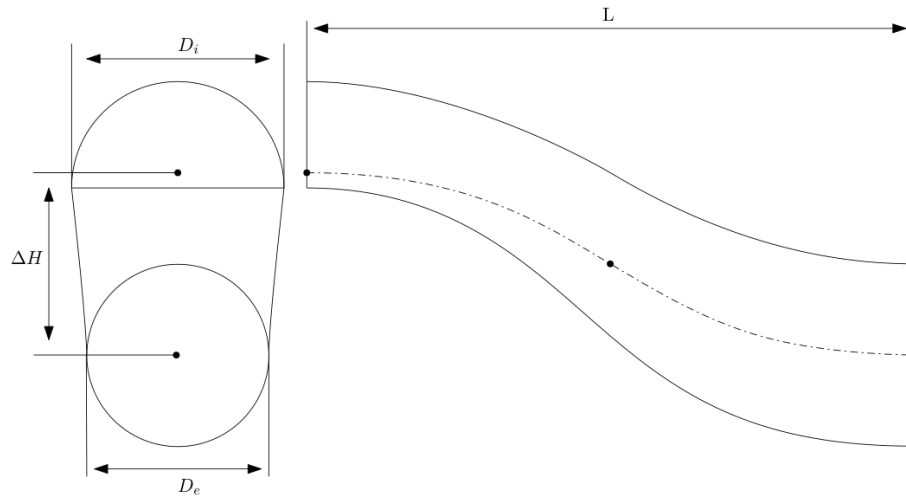


Figure 3.5: Geometry of the S-duct Inlet-Y.

The Inlet-Y is shown schematically in Figure 3.5. The geometry of Inlet-Y presents a semicircular inlet that transits into a circular outlet. This geometry presents an area ratio (A_e/A_i) equal to 1.07. It also presents a length-to-diameter ratio (L/D_e) equal to three and an offset (ΔH) equal to one output diameter. Table 3.5 summarises all the geometrically significant parameters of Inlet-Y.

Table 3.5: Inlet-Y overall geometry parameters.

Geometric Parameter	Reference Variable	Value
S-duct Length (m)	L	0.951
Inlet Diameter (m)	D_i	0.217
Inlet Area (m^2)	A_i	0.0619
Exit Diameter (m)	D_e	0.352
Exit Area (m^2)	A_e	0.0972
Centerline Shift (m)	ΔH	0.352
Length-to-Diameter Ratio	L/D_e	3.08
Centerline Shift Ratio	$\Delta H/D_e$	1.039
Area Ratio	A_e/A_i	1.069

Computational Domain

The computational domain is shown schematically in Figure 3.6. The domain includes the Inlet-Y and also an straight duct immediately after the Inlet-Y outlet section. The straight duct after the exit section, 6 exit diameters long, contains the AIP at one exit radius from the exit section of the Inlet-Y, the remaining 5.5 exit diameters are necessary to ensure that the boundary conditions in the outlet section of the domain do not affect the solution at the AIP. In fact, this distance was chosen by Frohnäpfel to avoid that the boundary conditions, imposed constant at the output of the domain, interact with the conditions at the AIP through the upstream signal propagations [4].

Unlike D'Ambros, it was decided not to add a cylindrical duct before the S-duct; in this way, instead of having a circular boundary layer developed by the cylindrical duct before the S-duct, a 2D boundary layer is imposed, which is closer to reality.

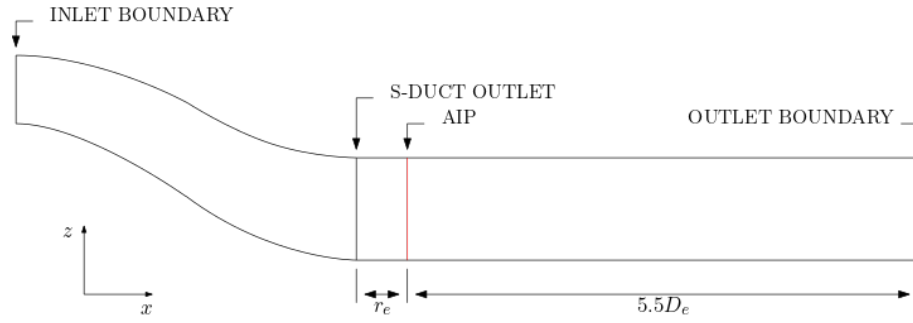


Figure 3.6: Geometry of the S-duct Inlet-Y.

Mesh Generation

As the previous geometry a Polyhedral Mesher was chosen for mesh generation, which creates an unstructured mesh with polyhedral-shaped cells Figure 3.7. In addition in Figure 3.7 it is possible to see prismatic cell layers next to the wall which allows the boundary layer to be captured accurately.

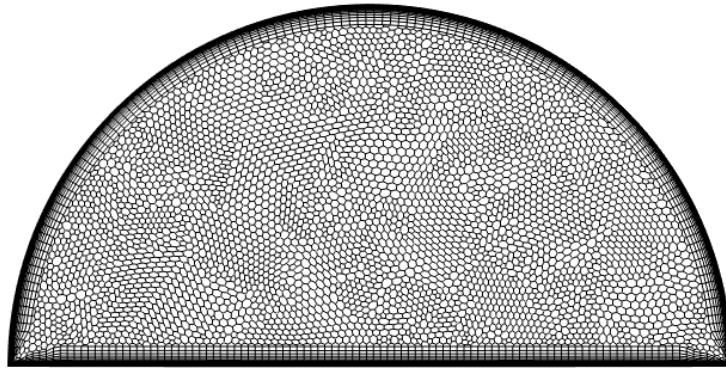


Figure 3.7: Mesh scene of the entrance section of Inlet-Y.

The thickness of the first layer was chosen to ensure a y^+ less than 1 throughout the duct. The total thickness of the prism layer was chosen to contain the boundary layer. The main characteristics of the mesh are summarised in Table 3.6.

Boundary Conditions

In the boundary conditions at the inlet of the Inlet-Y the ingestion of the boundary layer generated on the upstream aircraft was taken into account. For simplicity the inlet flow profile was simulated as a turbulent boundary layer in a flat plate. The

Table 3.6: Inlet-Y: mesh features.

Method	Unstructured Polyhedral Mesher
Target Surface Size (m)	0.005
Surface Growth Rate	1.1
Number of Prism Layers	30
Prism Layer Stretching	1.25
Prism Layer Total Thickness (m)	0.0136
Cells	7128141
Verts	22734844

turbulent boundary layer profile was approximated with the power law Eq. 3.8, deduced on experimental basis.

$$V_z = V_{z_\infty} \left(\frac{y}{\delta} \right)^{\frac{1}{7}} \quad (3.8)$$

V_z is the axial velocity component, V_{z_∞} represents the axial velocity outside the boundary layer, y is the spatial coordinate orthogonal to the wall and δ is the thickness of the boundary layer. In the simulation, a clean flow velocity (V_{z_∞}) of 193.7 m/s was considered. The thickness of the boundary layer is chosen to be 50% of the height of the S-duct inlet. In fact, in the literature it can be seen that this height for the boundary layer is representative, in terms of swirl distortion in the AIP, of reality. Figure 3.8 shows the normalised velocity profile at the S-duct inlet.

This velocity profile results in a mass flow rate of approximately 20 kg/s considering a static pressure and a total pressure of $1.0613 \cdot 10^5 \text{ Pa}$ and $1.0192 \cdot 10^5 \text{ Pa}$ respectively. The wall was defined as no-slip, smooth, stationary wall.

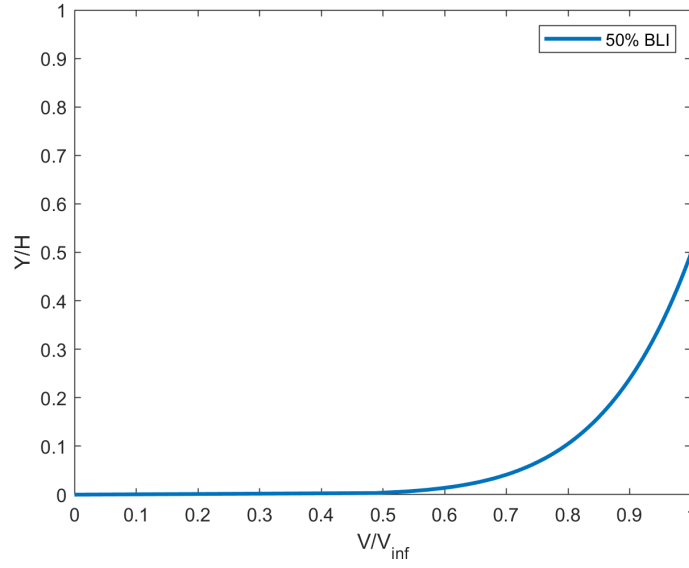


Figure 3.8: Turbulent Flat Plate Boundary Layer Profiles.

Convergence Criteria

It was considered necessary to have the RMS residual for the continuity, momentum, and energy equations below 10^3 as a convergence criterion. As shown in Figure 3.9, 13000 iterations are sufficient to satisfy this criterion.

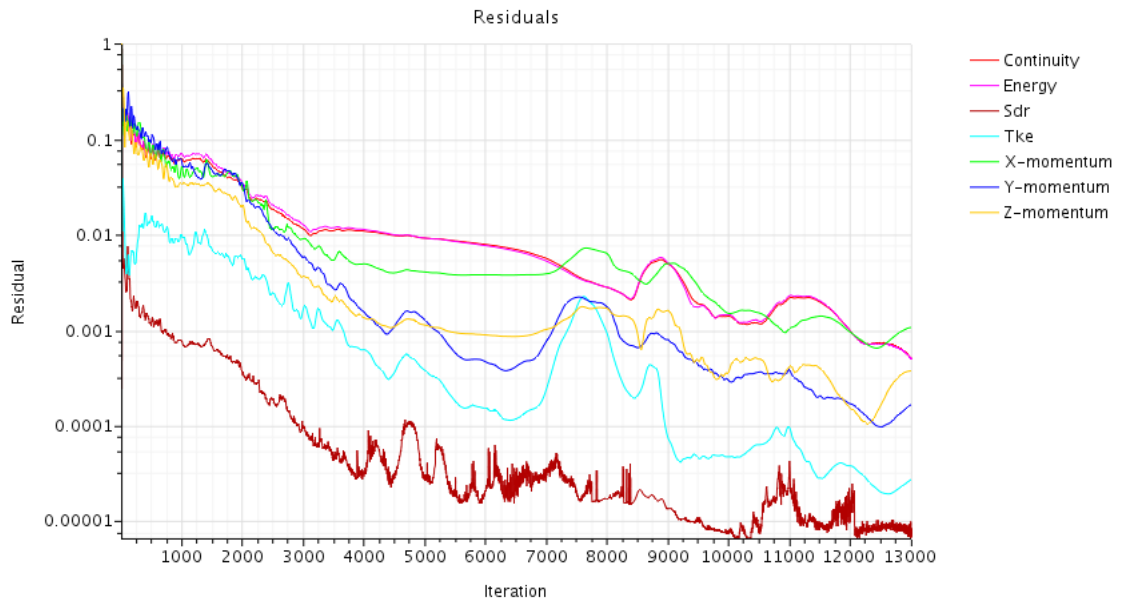


Figure 3.9: RMS residuals for Inlet-Y simulation.

3.1.3 Air Intake with Rectangular Inlet

Geometry

The third S-duct model chosen for the following study was developed by Chiang *etal.* [3] to study the effects of Aspect Ratio on S-duct performance. In the present work this S-duct is called Inlet-Z. Inlet-Z unlike Inlet-Y and Inlet X, which are readily available in the literature, represents a particular geometry that is rarely found in the literature. The geometry of Inlet-Z is shown schematically in Figure 3.10. The geometry of the Inlet-Z has a rectangular inlet which transits into a circular outlet. This geometry presents an area ratio (A_e/A_i) equal to 1.57. It also presents a length-to-diameter ratio (L/D_e) equal to about three and an offset (ΔH) equal to one output diameter. Table 3.7 summarises all the geometrically significant parameters of Inlet-Z.

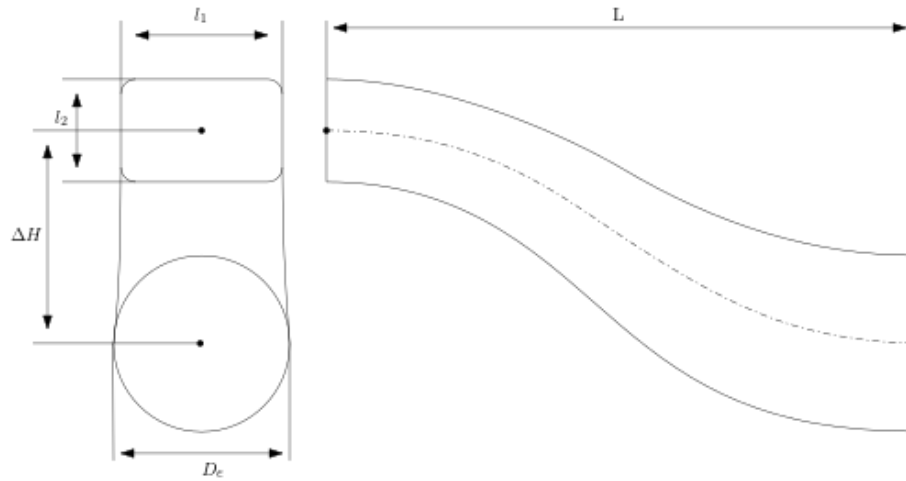


Figure 3.10: Geometry of the S-duct Inlet-Z.

Computational Domain

As in the case of Inlet-X, the domain consists of three ducts: the inlet duct, the S-duct and the outlet duct. The inlet duct is a straight rectangular-section duct with a length of eight radii, and it guides the airflow towards duct S. Downstream of the inlet duct stands the S-duct. The exit duct is located immediately after the S-duct and has a length of 6 radii. The exit duct contains the AIP, which is one exit radius downstream. Table 3.7 shows the geometric parameters of the computational

Table 3.7: Inlet-Z overall geometry parameters.

Geometric Parameter	Reference Variable	Value
S-duct Length (m)	L	0.951
Inlet Width (m)	l_1	0.217
Inlet height (m)	l_2	0.176
Inlet Area (m^2)	A_i	0.0619
Exit Diameter (m)	D_e	0.352
Exit Area (m^2)	A_e	0.0972
Centerline Shift (m)	ΔH	0.352
Length-to-Diameter Ratio	L/D_e	3.08
Centerline Shift Ratio	$\Delta H/D_e$	1.039
Area Ratio	A_e/A_i	1,57

domain as well as the geometric parameters characterising the S-duct.

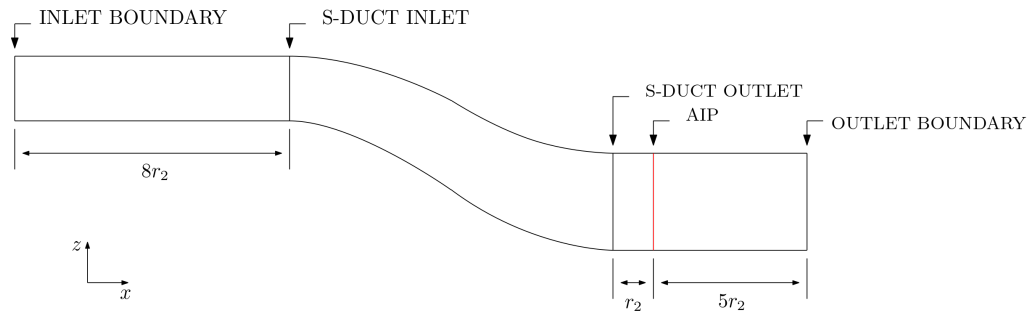


Figure 3.11: Sketch of the S-duct Inlet-Z Domain.

Mesh Generation

Also in this case, it was selected a Polyhedral Mesher for mesh generation, which creates an unstructured mesh with polyhedral-shaped cells, 3.12. In addition, Prism layer Mesher was used close to the wall in order to better simulate the boundary layer.

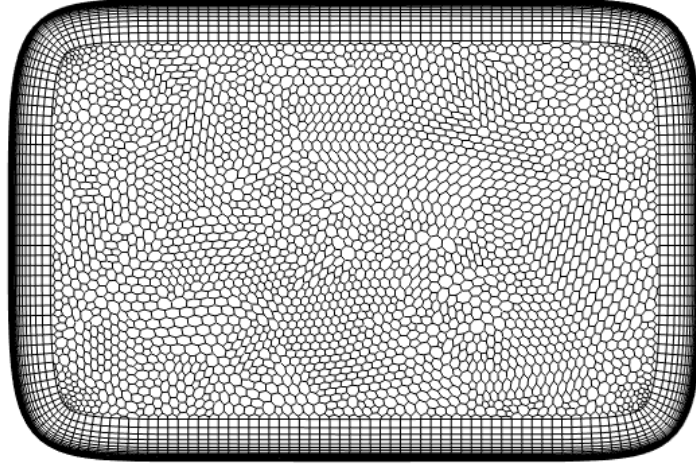


Figure 3.12: Mesh scene of the entrance section of Inlet-Z.

The thickness of the first layer was chosen to ensure a y^+ less than 1 throughout the duct. The total thickness of the prism layer was chosen to contain the boundary layer. The main characteristics of the mesh are summarised in Table 3.8.

Table 3.8: Inlet-Z: mesh features

Method	Unstructured Polyhedral Mesher
Target Surface Size (m)	0.005
Surface Growth Rate	1.1
Number of Prism Layers	35
Prism Layer Stretching	1, 25
Prism Layer Total Thickness (m)	0.0197
Cells	6674210
Verts	19433123

Boundary Conditions

The boundary conditions chosen for the simulation are those used by d'Ambros [5]. For the boundary conditions on Star CCM+, we imposed the inlet as Stagnation Inlet, and the outlet as Pressure Outlet, so for the boundary conditions we only

need the total and static pressure at the inlet while for the outlet we need the static pressure and the static temperature. The boundary conditions are collected in Table 3.9.

Table 3.9: Inlet-Z Boundary Conditions.

Parameter	Value
Inlet total pressure (Pa)	88744
Inlet static pressure (Pa)	69575
Outlet static pressure (Pa)	78982
Total temperature (K)	286,3

Convergence Criteria

It was considered necessary to have the RMS residual for the continuity, momentum, and energy equations below 10^{-3} as a convergence criterion. As shown in Figure 3.13, 10000 iterations are sufficient to satisfy this criterion.

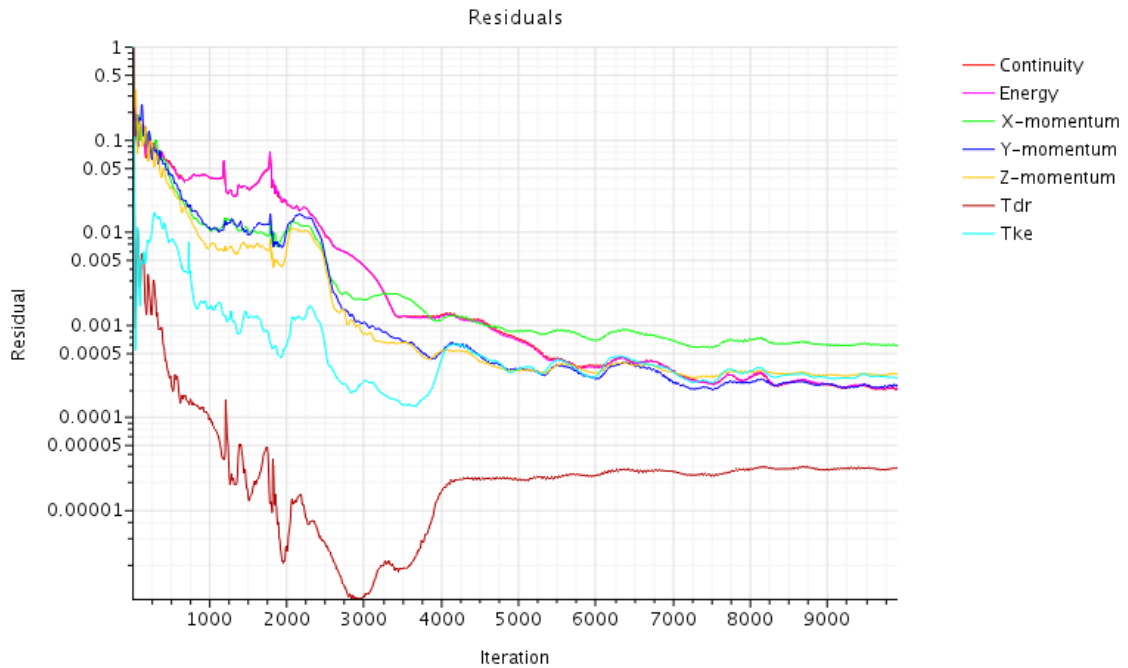


Figure 3.13: RMS residuals for Inlet-z simulation.

3.2 Inlet Duct Computational Results

The total pressure recovery factor and swirl angle will be used to characterise the flow inside the S-duct. The recovery factor is defined as follows:

$$R_0 = \frac{P_0}{\max(P_0)} \quad (3.9)$$

The recovery factor is therefore the ratio of the total pressure to the maximum total pressure in the plane being analysed. It is used to visualise how the total pressure evolves inside the duct, thus allowing to visualise possible separations caused by the geometry leading to the total pressure loss. The swirl angle is used to visualise and evaluate swirl distortions in the AIP. The swirl angle is formulated using Equation 3.10 with the terms of the equation defined in Figure 3.14.

$$\theta = \tan^{-1} \left(\frac{U_\theta}{U_x} \right) \quad (3.10)$$

Basically, the swirl angle is the angle between the tangential component, U_θ , and the axial component of the velocity, U_x , where the velocity is expressed in cylindrical coordinates. Thus the swirl angle represents the deviation of the flow from the purely axial configuration, the ideal condition, and is therefore directly related to the performance of the fan.

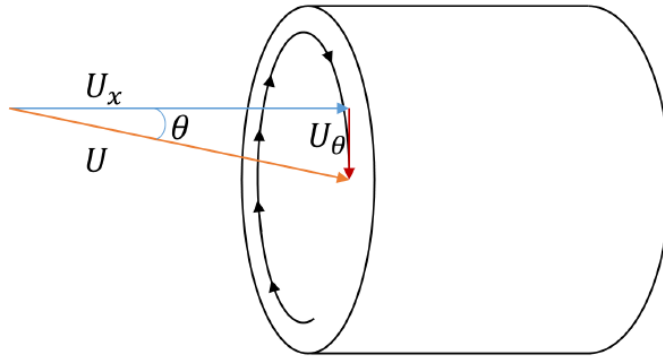


Figure 3.14: Swirl angle definition. [16]

3.2.1 Inlet-X Results

Figure 3.15 shows the profile of the total pressure recovery factor in the symmetry plane of Inlet-X. It can be seen from this profile that just after the first elbow the flow starts to separate in the lower wall. This separation causes a total pressure distortion to develop which sees a total pressure deficit in the lower part of the duct. After the second elbow a second separation starts to develop, the thickness of which is less.

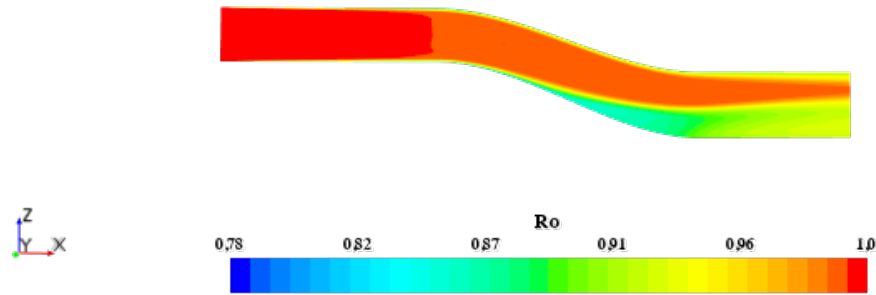


Figure 3.15: Inlet-X: Symmetry Plane Total Pressure Recovery Profile.

The separations that are established in this case are the main cause of the generation of secondary flows that lead to the development of transverse velocity components, leading to the formation of swirl distortions. Figure 3.16b shows the streamlines in the AIP together with the velocity countour in the plane. Through the streamlines it is easy to notice the presence of two counter rotating vortices in the lower part of the duct corresponding to the area affected by the total pressure deficit. In addition, it is possible to observe two further vortices confined near the wall in the upper part of the duct.

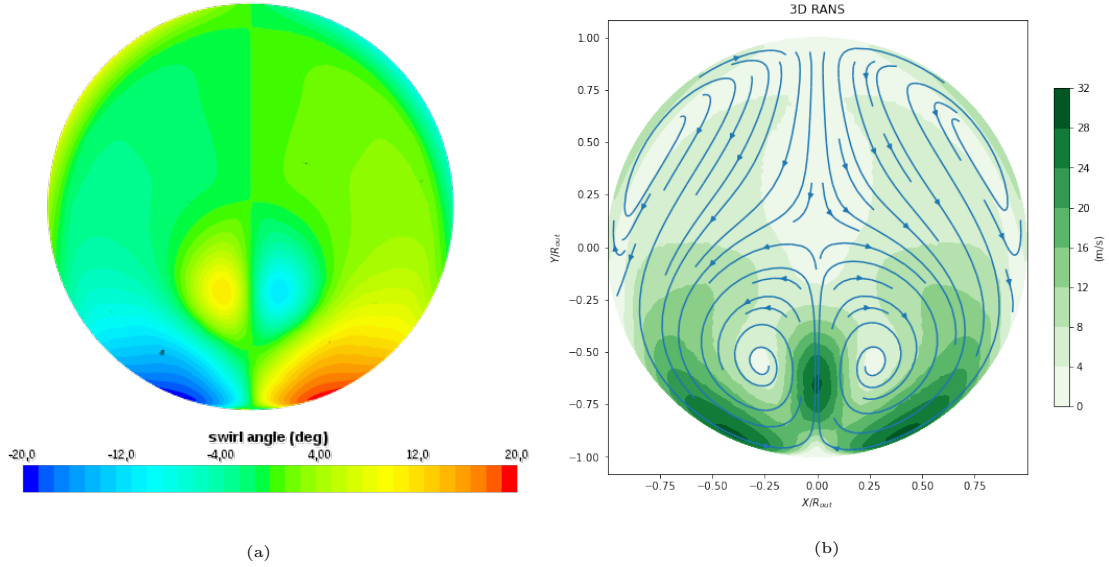


Figure 3.16: Inlet-X: swirl angle profile (a) and streamlines in the AIP (b).

Figure 3.16a shows instead the contour of the swirl angle in the AIP that confirm what was said before. Furthermore, through the contour of the swirl angle it is possible to state that the swirl distortion is more intense in the lower part of the duct. The solution obtained is in accordance with the results obtained in literature [11].

3.2.2 Inlet-Y Results

In Inlet-Y, as can be seen in Figure 3.17, there is no separation after the first elbow but only a slight thickening of the ingested boundary layer. After the second elbow (after the AIP) a second separation starts to develop.

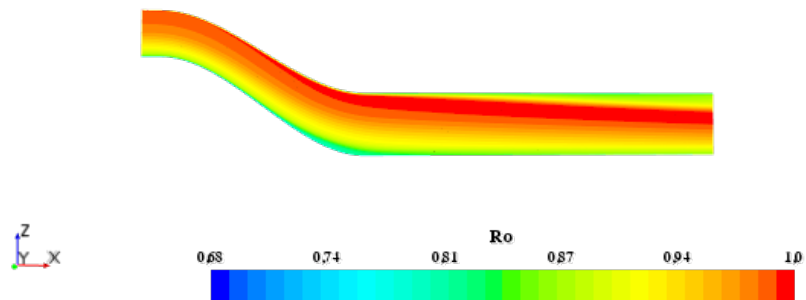


Figure 3.17: Inlet-Y: Symmetry Plane Total Pressure Recovery Profile.

The duct produces, as can be seen in Figure 3.18b, two counter-rotating vortices far apart and confined close to the wall. Figure 3.18a shows how the presence of the two counter-rotating vortices near the wall is characterised by a strong swirl angle convinced near the wall in the lower part of the duct. In reality the duct presents 4 vortices that are not detected in the AIP because the separation that is the cause of the two vortices position in the duct part occurs downstream of the AIP.

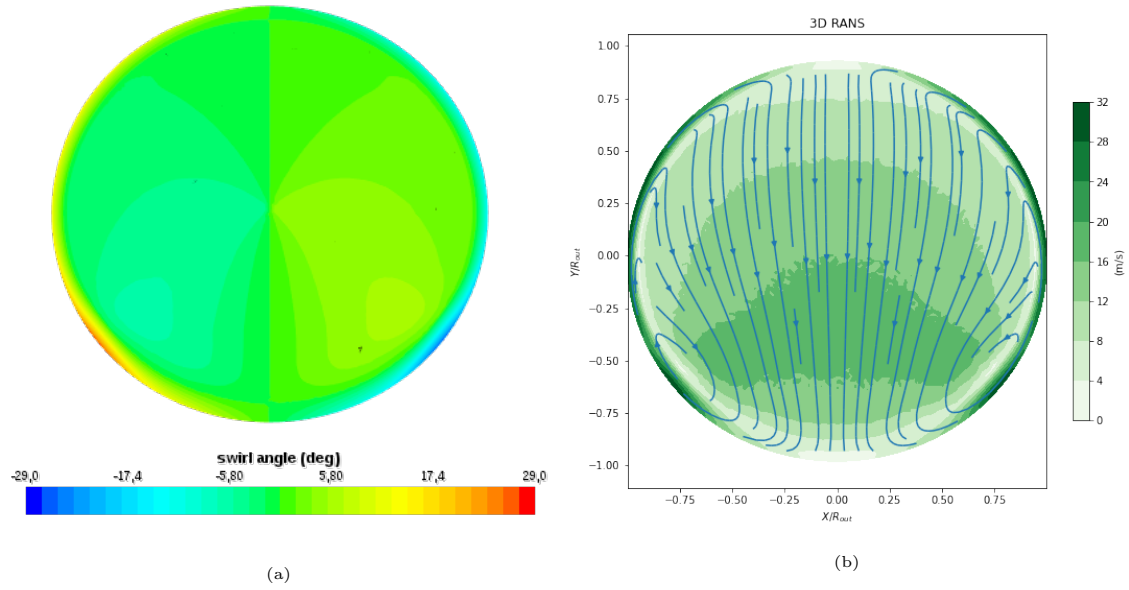


Figure 3.18: Inlet-Y: swirl angle profile (a) and streamlines in the AIP (b).

In order to obtain the same solution as Frohnapfel's [9], the same corrected flow rate was used, i.e. the same Mach. However, the solution found differs a bit from Frohnapfel's solution, which may be due to the difference in Reynolds compared to Frohnapfel's simulation.

3.2.3 Inlet-Z Results

Inlet-Z shows similar behaviour to Inlet-X. In Figure 3.19 it can be seen, in fact, that after the first elbow of the duct there is separation in the lower part of the duct. This separation causes a total pressure distortion at the exit of the duct. After the second elbow a second separation starts to occur. The two separations cause the formation of secondary flows which result in swirl angle distortions in the section of interest. Figure 3.20b shows how the configuration of vortices in the AIP, in this

case is more complex than in the previous jousts. In fact in this case there are six vortices created: two pairs of counter rotating vortices in the lower part of the duct and two vortices confined near the wall in the upper part of the duct. These vortices show a moderate swirl angle, Figure 3.20a, compared to the previous geometries.

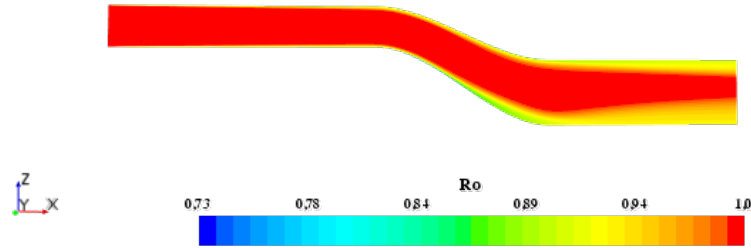


Figure 3.19: Inlet-Z: Symmetry Plane Total Pressure Recovery Profile.

The two separations cause the formation of secondary flows which result in swirl angle distortions in the section of interest. Figure 3.20b shows how the configuration of vortices in the AIP in this case is more complex than in the previous cases. In fact in this case there are six vortices created: two pairs of counter rotating vortices in the lower part of the duct and two vortices confined near the wall in the upper part of the duct. These vortices show a moderate swirl angle, Figure 3.20a, compared to the previous geometries.

The solution obtained seems to be in line with the solution obtained by Chiang et al. [3] before the duct optimisation.

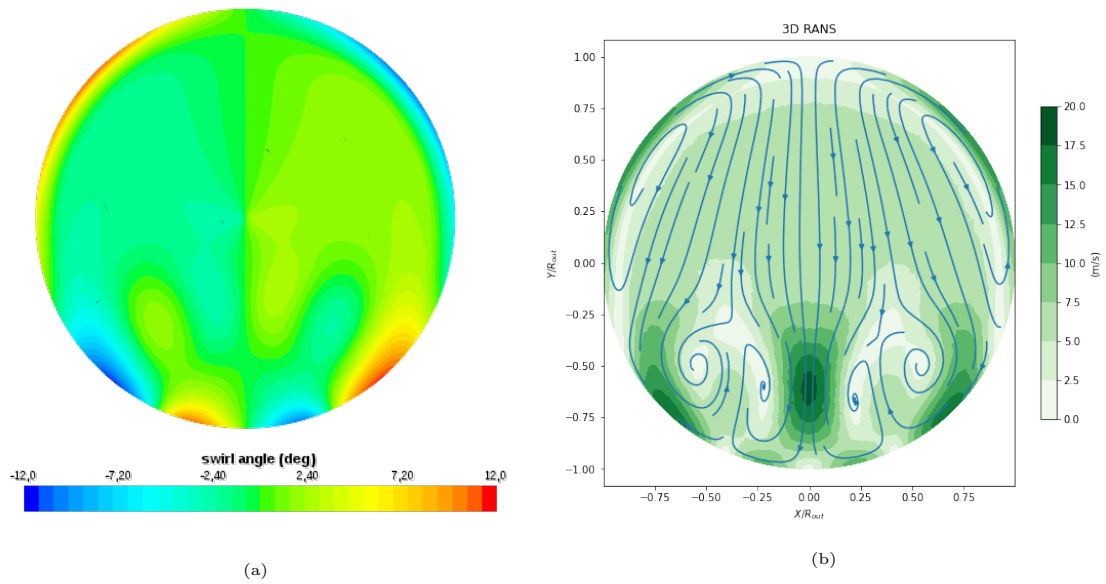


Figure 3.20: Inlet-Z: swirl angle profile (a) and streamlines in the AIP (b).

Chapter 4

Wishbone Computational Analysis

In this chapter, the behaviour of the baseline vortex generator type Wishbone is analysed computationally. The computational domain, the geometry considered, the flow conditions and the analysis settings are explained. This computational study serves to better understand the behaviour of the Wishbone vortex generator by means of inexpensive simulations, thus making it possible to predict the type of vortices generated and to understand the dynamics that lead to vortex generation. It is also essential to lay a solid basis for the parametric study that will serve to better adapt the distortion profile of the S-duct. For the following investigation, the vortex generator analysed is the one used experimentally by Wendt [38]. Unlike the study carried out by Wendt, the vortex generator is not installed in a flat surface but is inserted in a cylinder, in order to reproduce a computational domain similar to that of the previously analysed S-duct, which makes it possible to compare the results directly with those of the S-duct. Furthermore, the computational analysis was carried out on a scale and under flow conditions appropriate to the size and capacity of the test bench present in the Isae-Supaero experimental research laboratory, in order to validate this computational analysis at a later phase.

4.1 Wishbone Vortex Generator: Computetional Setup

4.1.1 Wishbone Vortex Generator Geometry

The Wishbone vortex generator used for the simulation was designed by Wendt et al.. Figure 4.1 shows the geometry of the Wishbone. Since we are interested in the generation of vortexes developing inside a duct in order to recreate the vortexes generated by the S-duct under boundary layer ingestion conditions, the studied geometry presents the Wishbone inside a cylindrical duct (Figure 4.2). The Table 4.1 shows the values of the geometrical parameters characterising the cylindrical duct and the baseline vortex generator.

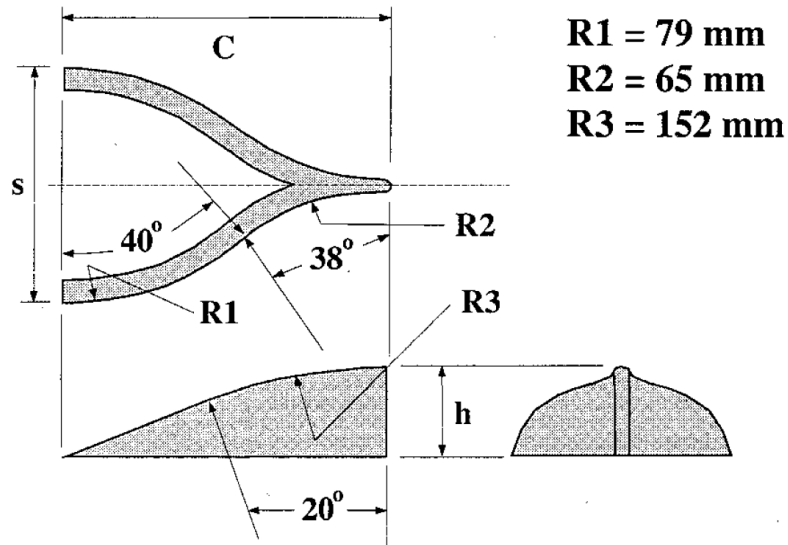


Figure 4.1: Wishbone Geometry. [38]

4.1.2 Computational Domain

To evaluate this method of generating swirl distortion, the Wishbone was computationally analysed, for simplicity, in an isolated configuration, therefore without considering the presence of the downstream fan. The computational domain consists in adding to the cylindrical duct containing the Wishbone shown in Figure 4.2 an additional cylindrical duct of length equal to one cylinder radius. Since the

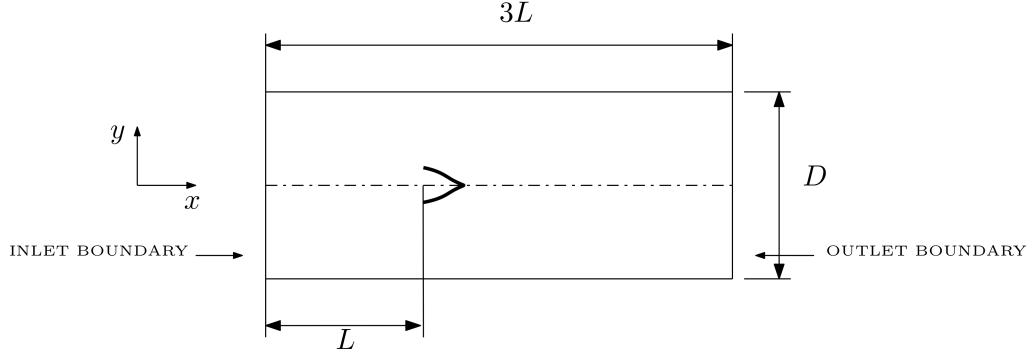


Figure 4.2: Wishbon domain.

AIP coincides with the outlet of the cylindrical duct containing the Wishbone, it has been chosen to add the outlet duct in order not to have interactions between the distortion profile at the AIP and the boundary conditions at the outlet of the domain. For reasons of computational cost and given the symmetry of the geometry with respect to the XZ plane, it was decided to perform the simulation only in half domain.

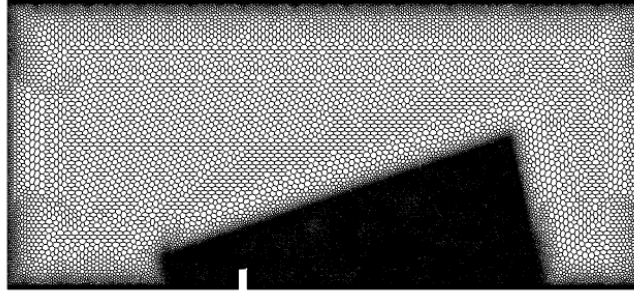
Table 4.1: Overall Wishbone geometry parameters.

Geometric Parameter	Reference Variable	Value
S-duct Length (m)	L	0.200
Duct Diameter (m)	D	0.352
VG height (m)	h	0.025
VG chord (m)	C	0.092
VG width (m)	s	0.068

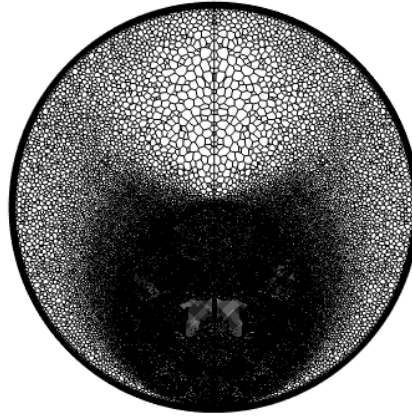
4.1.3 Mesh Generation

The Advancing Layer Mesher is used to discretize the computational domain by generating layers of prismatic cells around the surfaces of the domain, and filling the rest of the domain with polyhedral cells. Unlike the S-duct, the Polyhedral Mesher and the Prism Layer Mesher were not used because the Wishbone has edges that lead to anomalies in the generation of the prismatic layers, causing the simulations

to diverge. The thickness of the first layer was chosen to ensure a maximum y^+ equal to one. The total thickness of the prismatic layer was chosen to contain the boundary layer.



(a) Symmetry Plane



(b) AIP

Figure 4.3: Mesh scene in the symmetry plane and in the AIP.

To avoid computationally overloading the simulations it was chosen to have a coarse mesh in the region of the domain of no interest (i.e. the regions that are not affected by the Wishbone wake), which in the present analysis is called \mathcal{D} and to refine the mesh in the area of interest which is called \mathcal{V} . This was done by adding a Volumetric Control to incorporate the wake. To define the size of the Volumetric Control, a simulation was performed with a coarse mesh to identify approximately in which region the wake of the vortex generator develops. The Figure 4.3b shows the mesh scene in the symmetry plane and AIP. The parameters characterising the mesh are detailed in the Table 4.2.

The number of cells but especially the Surface Target Sizes come out from a mesh convergence study. Before being able to describe the mesh convergence study, it is

Table 4.2: Mesh features.

\mathcal{D}	
Method	Advancing Layer Mesher
Target Surface Size (m)	0.0025
Surface Growth Rate	1.3
Number of Prism Layers	25
Prism Layer Stretching	1, 25
Prism Layer Total Thickness (m)	0.00518
Cells	18923249
Verts	99203343
\mathcal{V}	
Method	Advancing Layer Mesher
Target Surface Size (m)	0.0011

necessary to define the Inlet Distortion Circumferential Coefficient (IDC). Equation 4.1 shows the definition of IDC. The definition of IDC is shown in the following equation:

$$IDC = \frac{1}{2} \max_{j \in \{1,2,3,4\}} \left\{ \frac{\hat{p}_{tj} - \min(p_{tj})}{\hat{p}_{t0}} + \frac{\hat{p}_{t_{j+1}} - \min(p_{t_{j+1}})}{\hat{p}_{t0}} \right\} \quad (4.1)$$

Where \hat{p}_{tj} is the average total pressure on the j – th circle, $\min p_{tj}$ is the minimum of the total pressure in the j – th circle and \hat{p}_{t0} is the average total pressure at the entrance of the domain. The pressures are calculated in concentric circles, of radius calculated through the Equation 4.2, belonging to the AIP.

$$r_{j+1}^2 = r_j^2 + \frac{R_s^2 - R_h^2}{N} \quad (4.2)$$

where R_s is the largest radius, R_h the smallest radius and N the number of circumferences. Figure 4.4 shows the relative IDC calculated as shown in Equation 4.3 as a function of the number of cells.

$$IDC_{rel} = \frac{IDC_i - IDC_f}{IDC_f} \quad (4.3)$$

The relative IDC was calculated as a function of the IDC of the finest mesh (IDC_f) that could be obtained with the available computational means. Analysing Figure 4.4 we see that the mesh with about 11 millions cells is a good compromise between an acceptable solution and a affordable computing power.

4.1.4 Physics Models

The physics models used are the same as those used for the S-Duct simulations seen in the previous chapter. For the sake of clarity, they are repeated in Table 4.3.

4.1.5 Boundary Conditions

The boundary conditions, summarised in the Table 4.4, were applied to match the capabilities of the test bench.

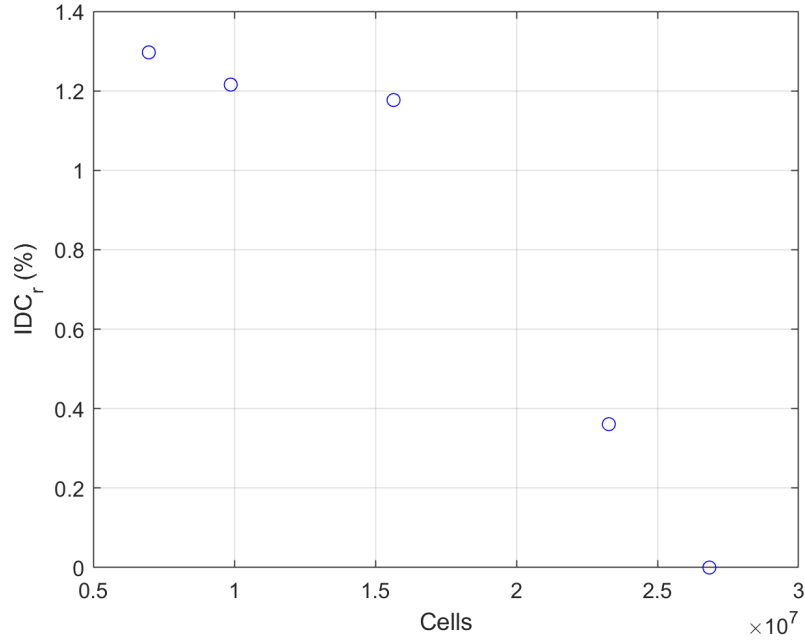


Figure 4.4: Mesh convergence.

Table 4.3: Physics Models for Wishbone Simulations.

Physics Models.
Ideal Gas
Steady
Coupled Flow Models with Coupled Energy Extension
Turbulent Boundary Layer
k- ϵ
Total temperature

4.1.6 Simulation Results

The flow interacting with the vortex generator was also characterised through the swirl angle and the Total Pressure Recovery Factor. As mentioned above, the simulations were only conducted in half a domain, so the solution is presented only for half a duct. Figure 4.5b is a plot of the streamlines in the AIP plane and also shows the contour of the velocity component in the plane. Observing the figure,

Table 4.4: Wishbone Domain Boundary Conditions.

Parameter	Value
Inlet total pressure (Pa)	108775,8
Inlet static pressure (Pa)	101325
Outlet static pressure (Pa)	101325
Total temperature (K)	294

it can be seen that the Wishbone generates two counter-rotating vortices. These vortices can also be seen in Figure 4.5a, which shows a contour of the swirl angle in the plane of the AIP. In addition, it is possible to observe the presence of two more counter-rotating vortices, of lower intensity, confined near the wall in the lower part of the duct.

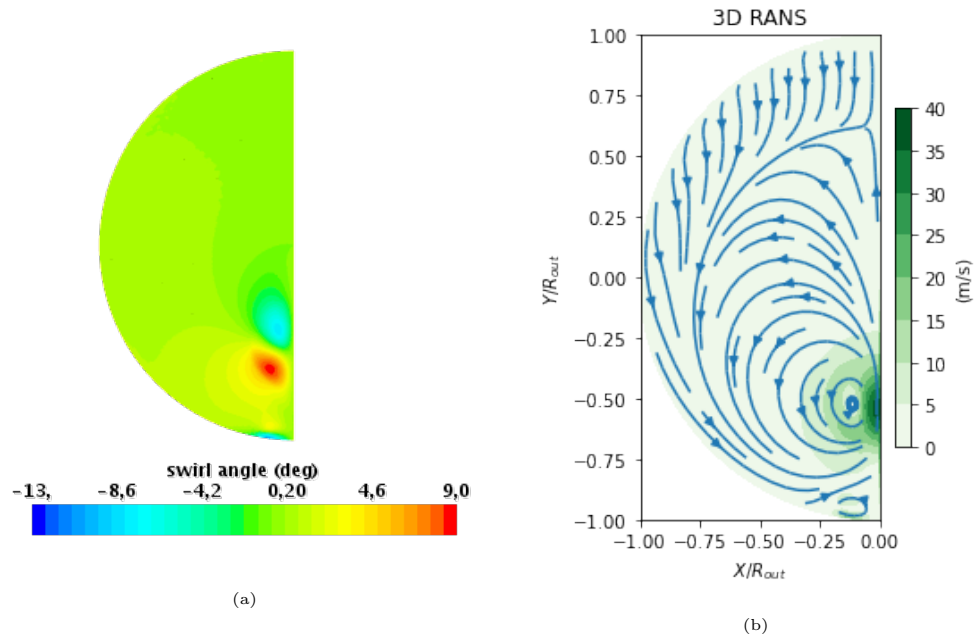


Figure 4.5: Inlet-Y: swirl angle profile (a) and streamlines in the AIP (b).

In Figure 4.6 the evolution of the flow interacting with the Wishbone is depicted. The Wishbone can be seen as two symmetrical wings glued together. The flow, arriving from the left, is accelerated and deflected by one of the two wings of the Wishbone, leading to the formation of the vortical structures. The two vortices that

begin to form at the tip of the two wings begin to thicken and separate from the wall moving towards the top of the duct. The clean flow, which does not interact with the Wishbone, causes the two vortices to curve, tilting in the direction of the clean flow.

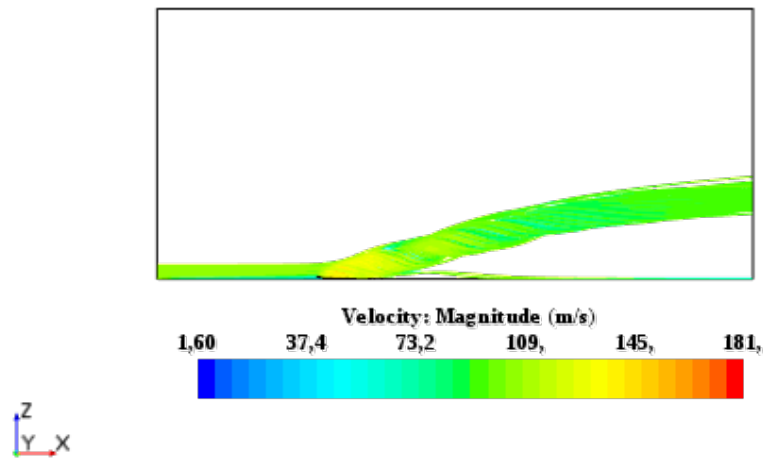


Figure 4.6: Representation of the evolution of streamlines, arriving from the inlet, interacting with the Wishbone.

Chapter 5

Vortex Sensitivity to Geometric Parameters

In this chapter a parametric analysis will be conducted on the wishbone geometry presented in Chapter 4, which allows for a better understanding of how the swirl angle pattern in the AIP is affected by the geometric parameters. Furthermore, this parametric study allows us to understand the limitations of this method for vortex generation and we will try to explain what these limitations are. This parametric study will therefore allow a preliminary understanding of what types of swirl distortions can be reproduced. For this analysis, the height (h), width (s) and chord (C) of the Wishbone will be varied. For simplicity, the parameters are changed independently of each other.

5.1 Parametric Study Setup

The geometry of the Wishbone (Figure 4.1) is mainly characterised by three parameters: the height (h), the width (s) and the chord (C). In order to evaluate the influence of these parameters on the wake of the Wishbone, they will be varied with a constant step within a certain range. The influence of each individual parameter will be treated independently of the others. The simulations with the various geometries are discretized with a mesh that preserves the characteristics of

the one used for the analysis of the baseline geometry. Furthermore, the boundary conditions, physical models and fluid properties have been kept unchanged. Table 5.1 summarises for each parameter the upper and lower limit and the step.

Table 5.1: Definition of parameter variation ranges.

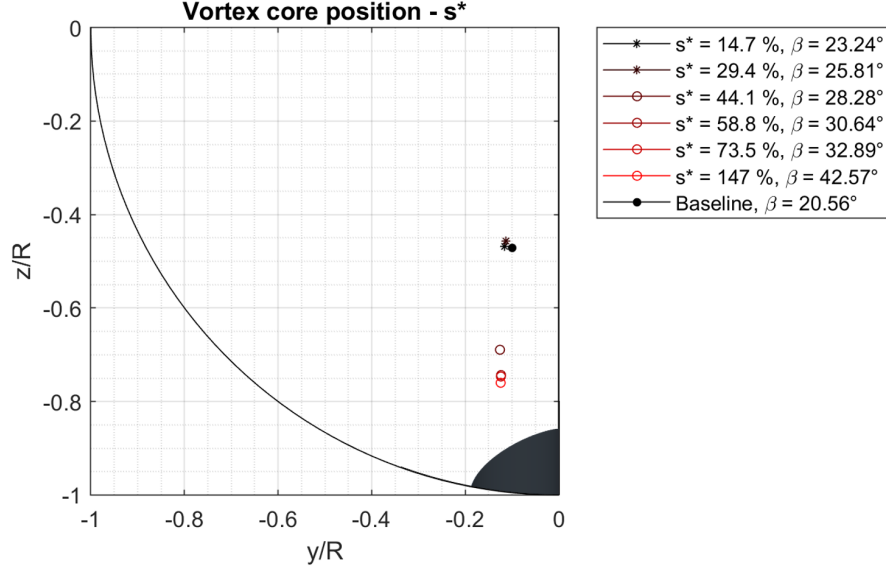
Factor	Lower Limit	Upper Limit	Step	Baseline	Additional Value
Δs (mm)	10	50	10	$s = 68$ mm	100
ΔC (mm)	10	50	10	$C = 92$ mm	-
Δh (mm)	-10	-2	2	$h = 25$ mm	-

5.2 Influence of the VG Width

Firstly, the impact of the width (s) on the position of the vortexes was analysed. Figure 5.1 shows the vortex core positions as a function of the parameter s^* which is simply s scaled by $s_{baseline}$. In the Figure 5.1, only a quarter of the duct that is affected by the presence of the vortices is shown. To each s^* corresponds a certain β which is defined as follows:

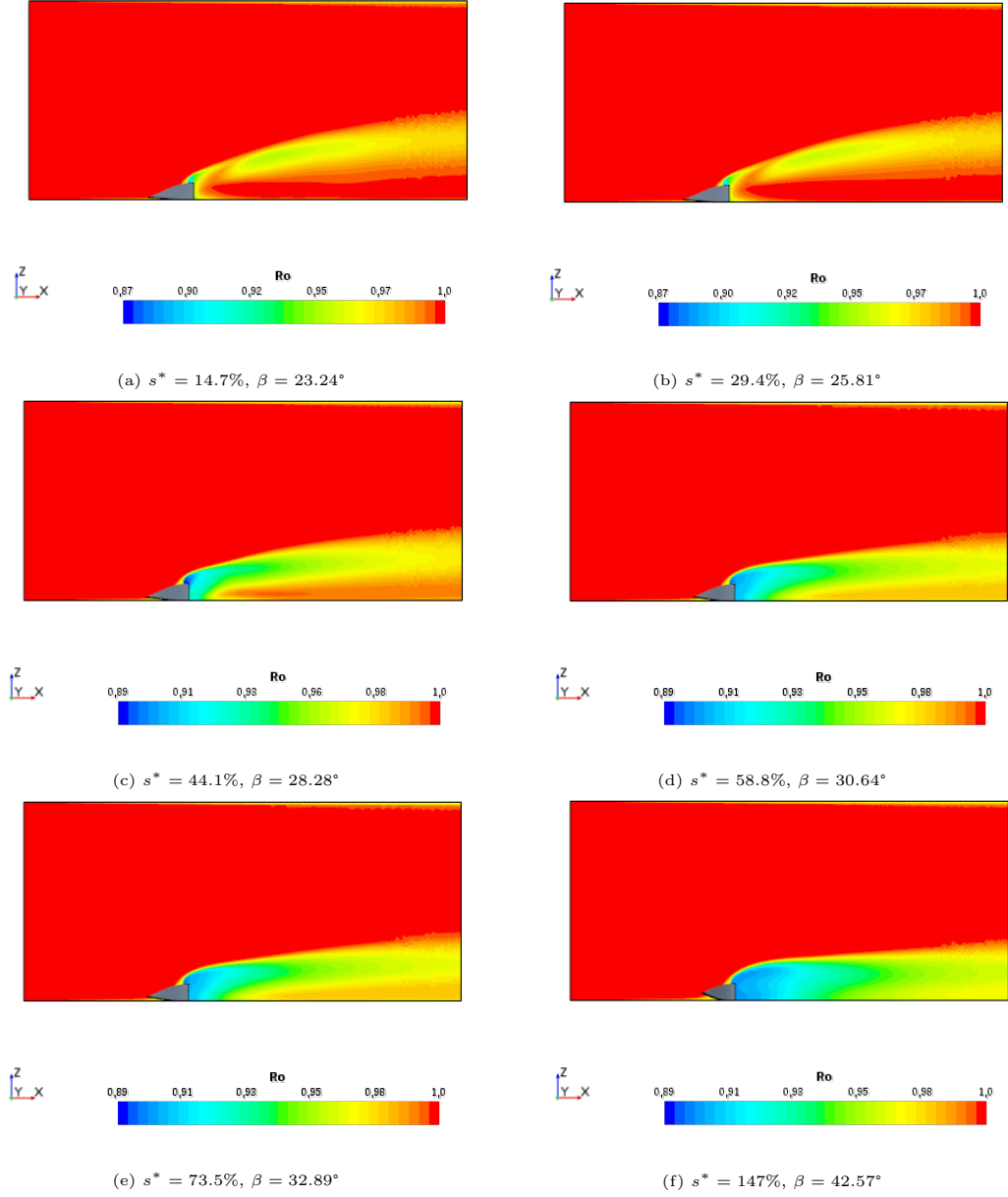
$$\beta = \arctan\left(\frac{2C}{s}\right) \quad (5.1)$$

so β is nothing else than the angle between a Wishbone wing and the plane of symmetry. The first feature that can be noticed is that s does not affect the horizontal position of the vortex core, which seems to stay constant. As for the vertical position of the vortex core, it can be seen that initially, moving away from the baseline, then increasing s and then β , there is a slight, almost negligible, upward movement. While starting from $s^* = 44.1\%$ there is an abrupt translation of the vortex core downwards. Increasing s even more we notice that the vortex continues to move downwards. Starting from $s^* = 58.8\%$ and thus $\beta = 30.64^\circ$ the influence of s^* becomes negligible. To better understand what this behaviour is due to we need to analyse Figure 5.2 which shows the recovery factor in the symmetry plane. It can be

Figure 5.1: Position of the vortex core as a function of s^* .

seen that for the cases in Figure 5.7a and Figure 5.10a, as in the case of the baseline, the vortex starts to form from the end of the VG wing and moves upwards and then is curved by the clean flow arriving from the inlet. While starting at $s^* = 44.1\%$ which corresponds to an angle $\beta = 28.28^\circ$ between the flow and the Wishbone wing, the flow begins to separate. The separation creates a more or less large recirculation zone, which size depends on the angle β . The recirculation zone tends to delay the creation of the two counter-rotating vortices, which results in less intense vortices that cannot move upwards because the clean flow does not allow it.

Figure 5.3 shows the contour of the swirl angle in the AIP as a function of s^* . It can be seen that initially increasing s^* and thus β results in a slight increase of the swirl angle. While when the recirculation zone starts to form, besides noticing a downward translation of the vortex, one notices that there is also a sharp reduction of the swirl angle. By increasing s^* even more, an increase of the swirl angle is noticed. This does not mean that the intensity of the vortex is increasing. In fact, as shown in Figure 5.1, which shows how the maximum of the axial component of the vorticity varies as a function of the parameter s^* , by increasing s^* the maximum of vorticity at the vortex core decreases. The increase of the swirl angle is due to the movement of the vortex at the wall which causes a reduction of the axial velocity

Figure 5.2: R_0 contour in the symmetry plane.

increasing the value of the swirl angle.

5.3 Influence of the VG Chord

For the analysis of the influence of the parameter C , we chose to analyse a range of values that would not give the same β values as those in the analysis of the parameter s , because we would have very similar solutions. To analyse the results we must first define the parameter c^* which is simply the C to $C_{baseline}$ ratio. Figure

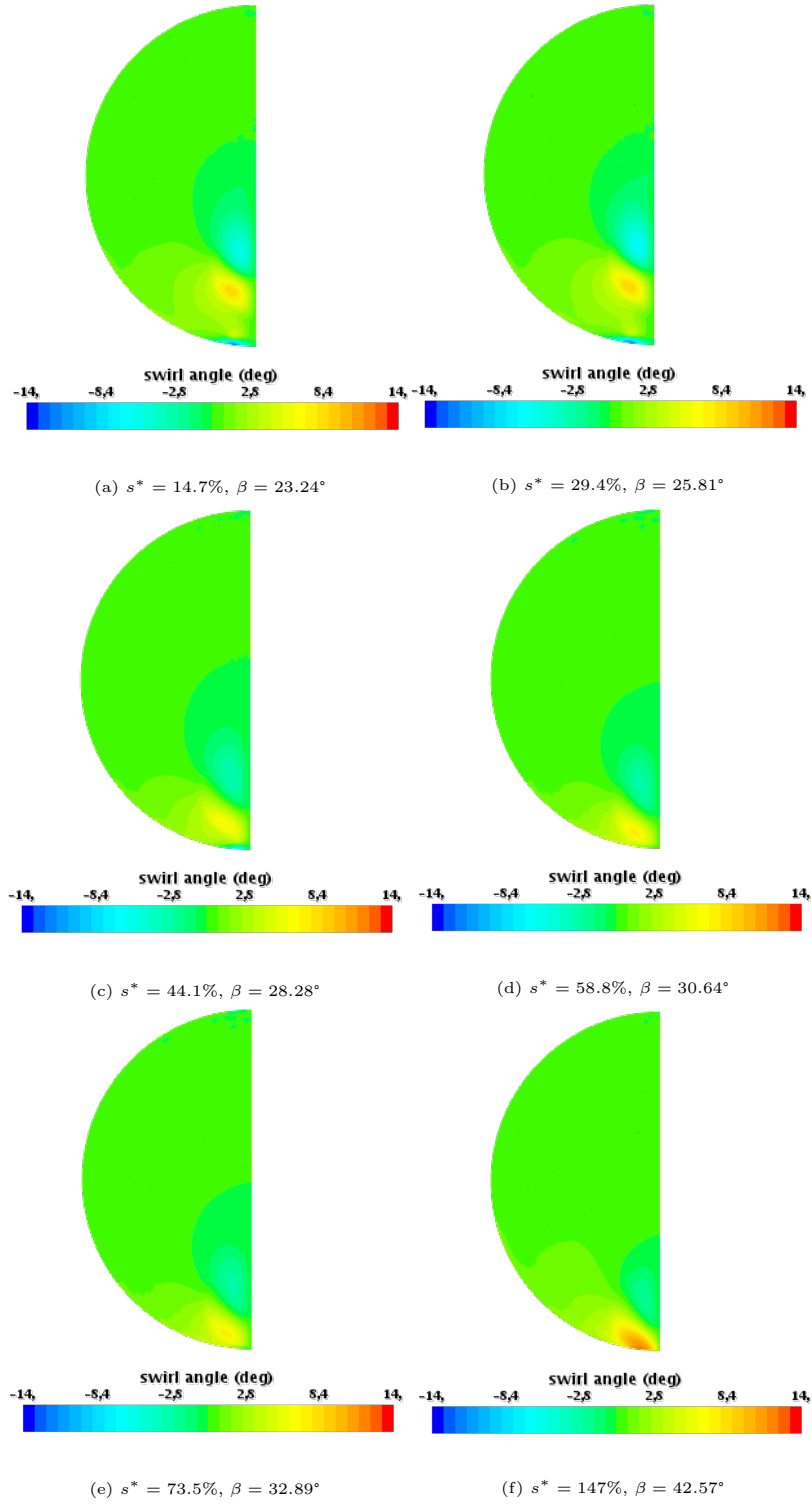
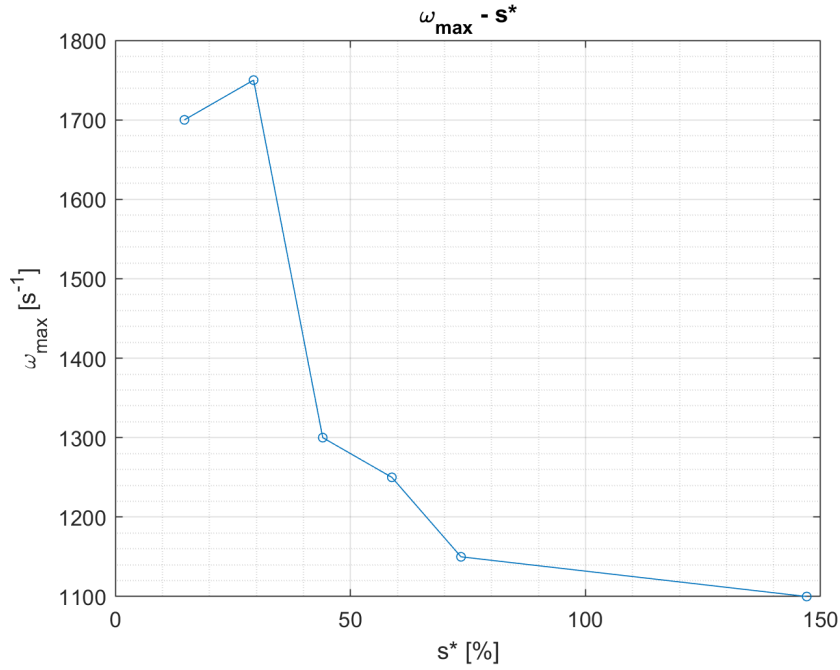
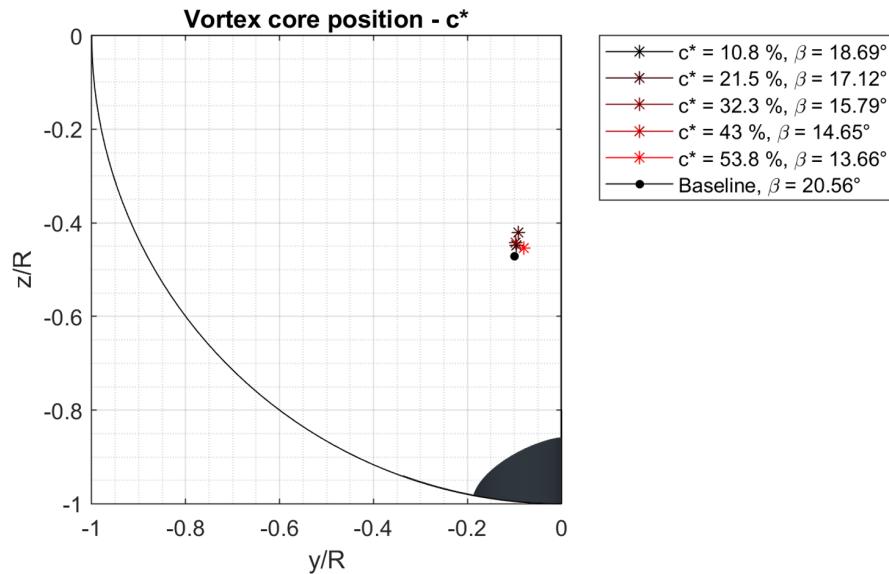


Figure 5.3: Swirl angle contour.

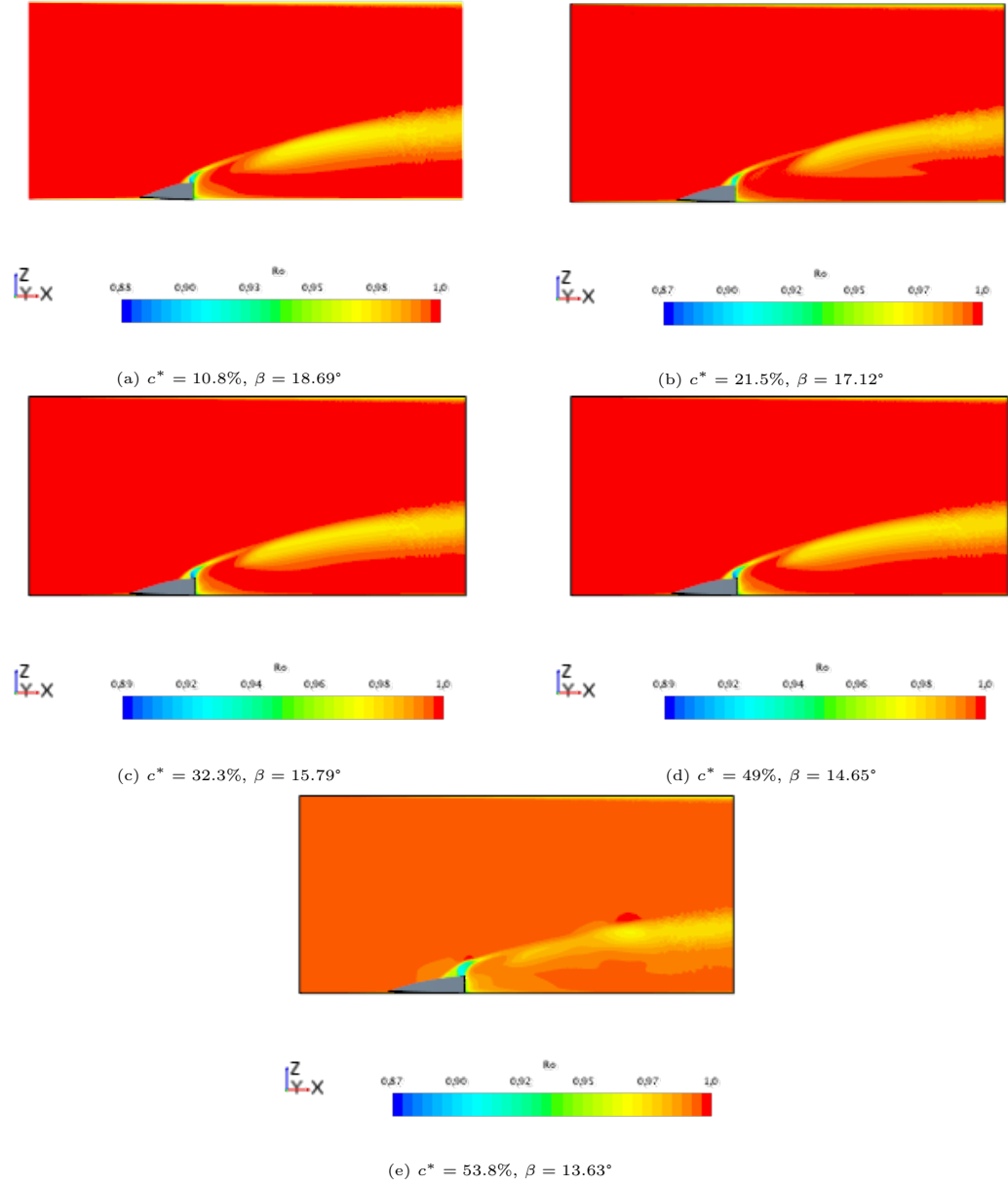
5.5 shows how the increase of c , hence the reduction of β below the value for which the recirculation zone is formed, does not affect either the horizontal or the vertical position of the vortex core. As Figure 5.6 shows how in all cases the vortices

Figure 5.4: Maximum axial vorticity as a function of the parameter s^* .

are generated immediately downstream of the vortex generator without any presence of recirculation zones since in all cases we are below the β for which a recirculation zone is formed, which is about 28° .

Figure 5.5: Position of the vortex core as a function of c^* .

The increase of c also leads to an increase in the intensity of the two vortices which results in an increase of the swirl angle and the maximum of the axial vorticity, as

Figure 5.6: R_0 contour in the symmetry plane.

shown in Figures 5.7 and 5.8.

5.4 Influence of the VG height

To complete the parametric study, the height of the vortex generator was also varied. Unlike the previous cases, in this case h has been reduced, since by increasing it, starting from Δh equal to 3 mm, a recirculation zone is generated downstream of the vortex generator equal to a radius of the duct that increases as h increases, this

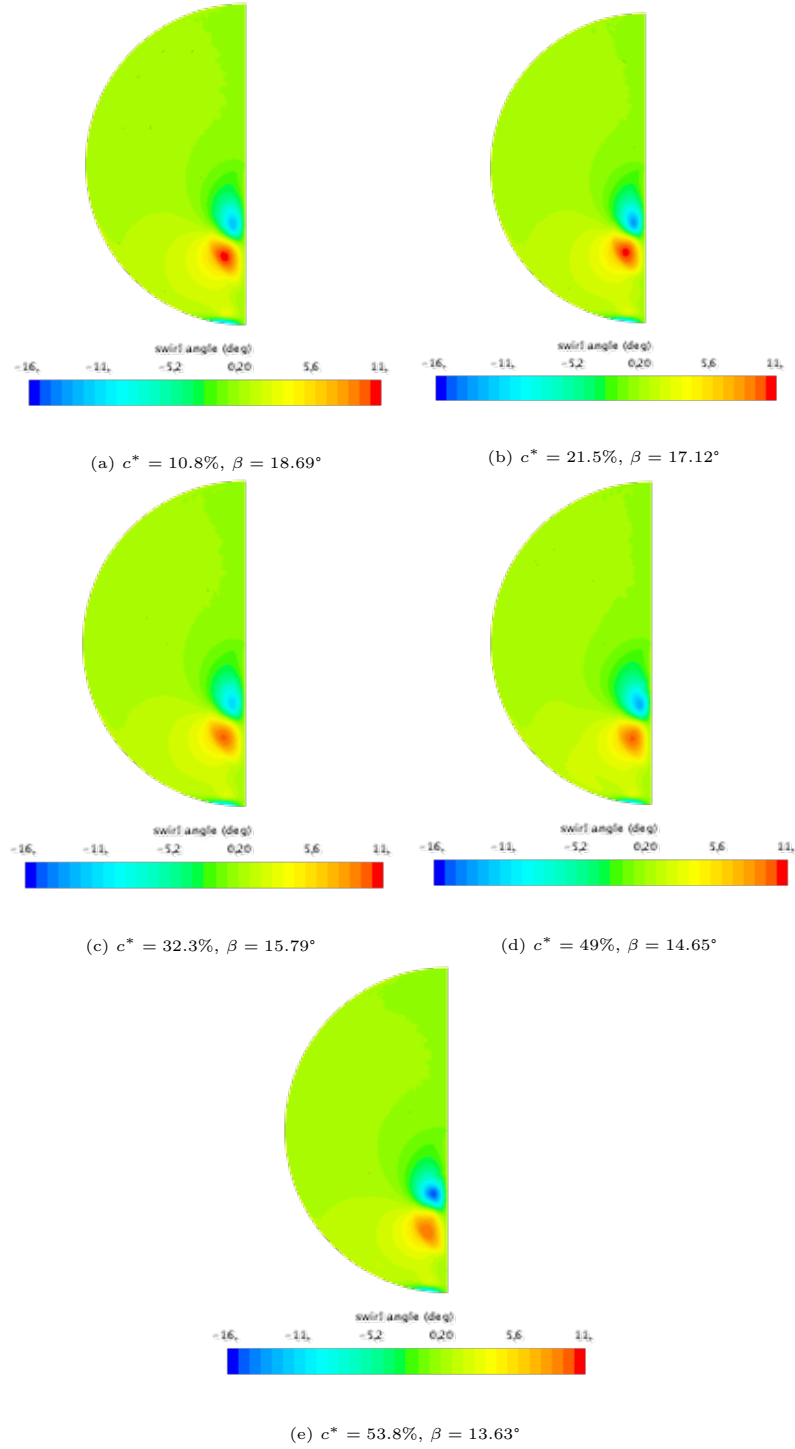


Figure 5.7: Swirl angle contour.

causes the delay of vortex generation, and this results in the absence of vortices in the AIP. To analyse the influence of h we define h^* which as in the previous cases is the ratio of h to $h_{baseline}$. From Figure 5.9 one can see that a reduction results in a slight translation of the vortex core downwards, while the horizontal translation

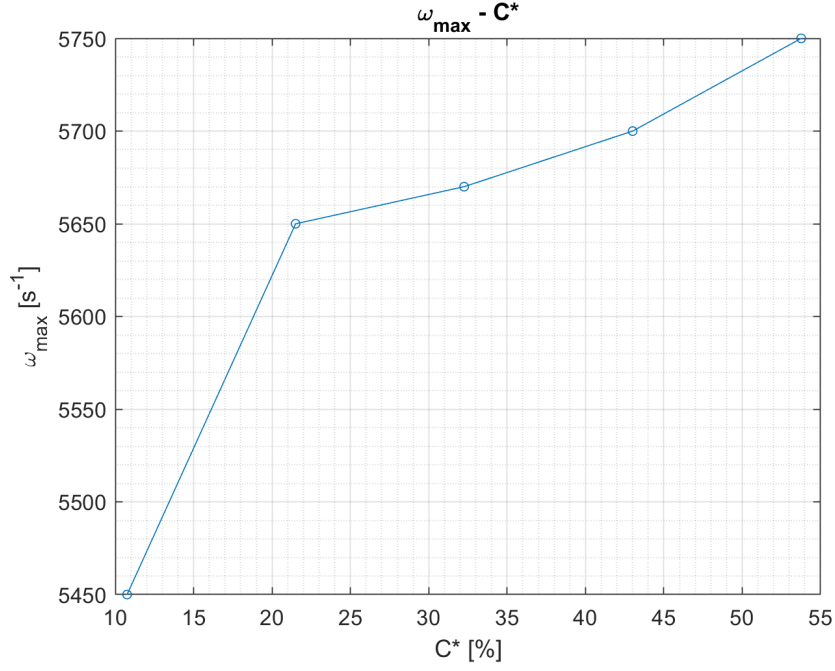


Figure 5.8: Maximum axial vorticity as a function of the parameter c^* .

continues to be negligible.

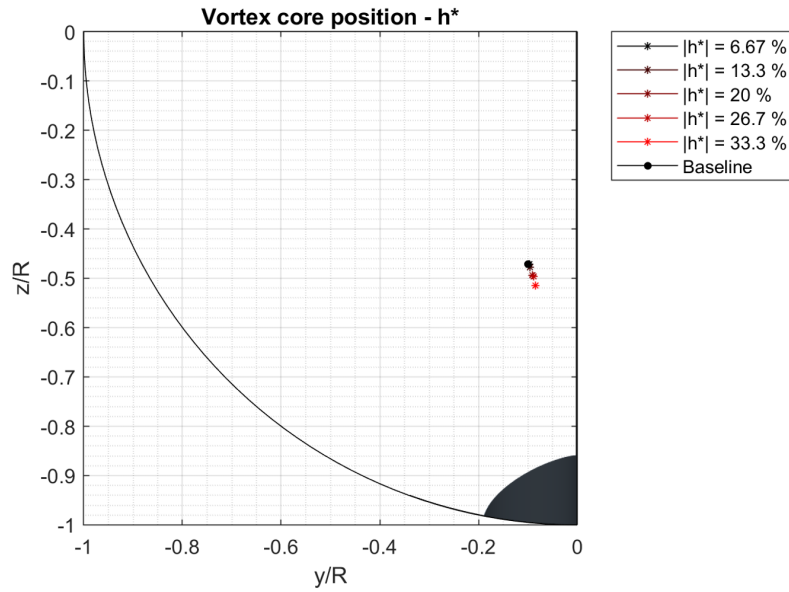


Figure 5.9: Position of the vortex core as a function of h^* .

Figure 5.10 shows the pattern of the swirl angle as h varies. It can be seen that the variation of the swirl angle is almost negligible.

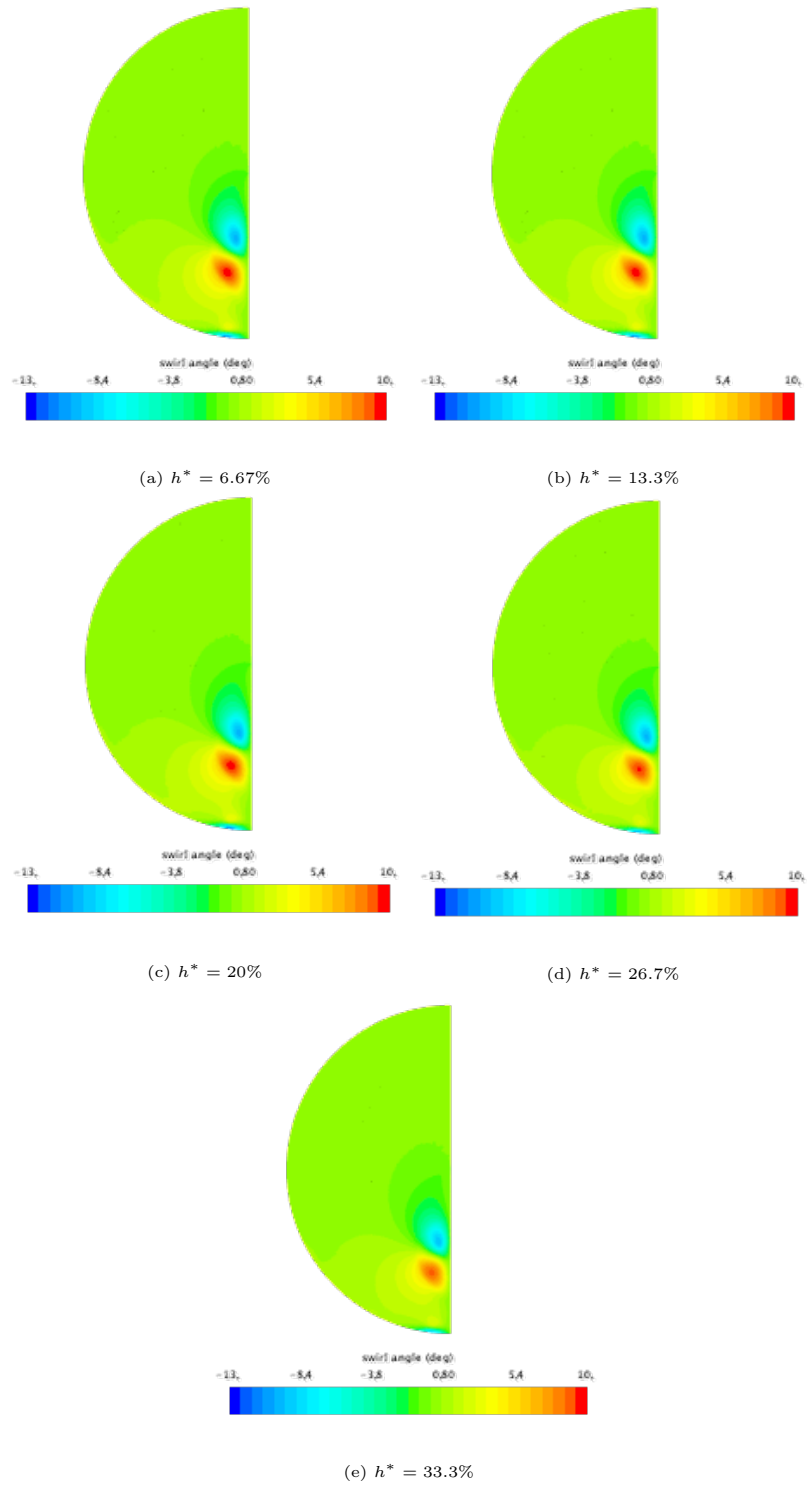


Figure 5.10: Swirl angle contour.

Chapter 6

Conclusions and Future Work

6.1 Research Outcome and Discussion

Inlet flow distortions are a major contributor to airframe/engine incompatibilities. Distortions can be of several types, but the ones that most degrade engine performance are pressure and swirl distortions. Performance analysis using only total pressure distortions is not sufficient. In fact, in many airframe/engine configurations, it is mandatory to analyse the effects of swirl distortion in order to certify operability and performance. In the literature there are several methods for the generation of swirl distortions that are more or less complicated. In this paper, a new method for the generation of swirl angle distortions is analysed, which consists in the use of vortex generators, more precisely Wishbone. A parametric study has been conducted to observe how different geometrical parameters influence the pattern of the two counter-rotating vortices generated by the Wishbone. This work therefore serves as the basis for a possible geometric optimisation to adapt the two vortices to reproduce the typical swirl distortion of S-duct. In order to better analyse the results obtained by the Wishbone, three S-duct geometries have been computationally simulated, which differ in their inlet geometry. These geometries have been analysed because they present 3 different types of swirl angle patterns and are very similar to the S-duct that is planned to be integrated into new aircraft designs. The parametric study showed the different limitations of this method.

A first limitation is the little influence of the geometrical parameters on the in the x-axis position of the vortices. This limitation makes the use of the Wishbone very limited, in fact it greatly reduces the swirl distortion patterns that can be reproduced. For example, all three swirl distortion patterns obtained with the three different S-duct geometries cannot be reproduced through the Wishbone because the position of the vortices with respect to the symmetry plane is greater than that of the vortices generated by the Wishbone.

The second limitation is related to the number of vortices generated by the Wishbone. In fact, as seen in the three S-duct analysed, there are configurations with more than two vortices that could not be reproduced by the Wishbone. More wishbones could be added in a duct in order to increase the number of vortices, but the first limitation persists so also in this case the distortions obtained in the S-duct could not be reproduced. The vertical position of the vortex seems to be controlled through the height of the Wishbone and by β (thus by s and by C) but again there are limitations.

Concerning the swirl angle, the three parameters show some influence on it but not excessive. In fact by varying the parameters the swirl angle varies only by a few degrees. So it can be concluded that through the Wishbone it is possible to reproduce swirl distortions but the configurations that can be reproduced are limited. This study therefore serves to understand the limits of the Wishbone for distortion generation. In the literature, besides the Wishbone, there are other vortex generators that would allow us to bypass these limits and create more complex distortion patterns. One could also use multiple types of vortex generators to create increasingly complex distortions. Then you could analyse how these vortex generators work and then optimise the geometry of each one to obtain the desired distortion pattern.

Bibliography

- [1] Asad Asghar, Robert A Stowe, William DE Allan, and Derrick Alexander. Entrance aspect ratio effect on s-duct inlet performance at high-subsonic flow. *Journal of Engineering for Gas Turbines and Power*, 139(5), 2017.
- [2] ZhanJun Chen and JinJun Wang. Numerical investigation on synthetic jet flow control inside an s-inlet duct. *Science China Technological Sciences*, 55(9):2578–2584, 2012.
- [3] Christopher Chiang, David Koo, and David W Zingg. Aerodynamic shape optimization of an s-duct intake for a boundary layer ingesting engine. In *AIAA AVIATION 2021 FORUM*, page 2468, 2021.
- [4] Milt Davis, Alan Hale, and Dave Beale. An argument for enhancement of the current inlet distortion ground test practice for aircraft gas turbine engines. *J. Turbomach.*, 124(2):235–241, 2002.
- [5] Alessio D’Ambros, Timoleon Kipouros, Pavlos Zachos, Mark Savill, and Ernesto Benini. Computational design optimization for s-ducts. *Designs*, 2(4):36, 2018.
- [6] S Farokhi. Propulsion system design with smart vortex generators. *Aircraft Design*, 1(3):127–143, 1998.
- [7] Anthony Ferrar, William Schneck, Justin Bailey, Kevin Hoopes, and Walter O’Brien. Application of additive manufacturing to rapidly produce high-resolution total pressure distortion screens. In *50th AIAA Aerospace Sciences Meeting including the New Horizons Forum and Aerospace Exposition*, page 929, 2012.

- [8] JE Flitcroft, J Dunham, and WA Abbott. Transmission of inlet distortion through a fan. Technical report, ROYAL AIRCRAFT ESTABLISHMENT FARNBOROUGH (UNITED KINGDOM), 1987.
- [9] Dustin Joseph Frohnepfel. *Methodology Development and Investigation of Turbofan Engine Response to Simultaneous Inlet Total Pressure and Swirl Distortion*. PhD thesis, Virginia Tech, 2019.
- [10] HP Genssler, W Meyer, and L Fottner. Development of intake swirl generators for turbo jet engine testing. Technical report, MESSERSCHMITT-BOELKOW-BLOHM GMBH MUNICH (GERMANY FR) HELICOPTER AND MILITARY . . . , 1987.
- [11] Daniel Gil-Prieto, David G MacManus, Pavlos K Zachos, Geoffrey Tanguy, and Kevin R Menzies. Convolutional intake distortion measurements using stereo particle image velocimetry. *AIAA Journal*, 55(6):1878–1892, 2017.
- [12] RW Guo and J Seddon. An investigation of the swirl in an s-duct. *Aeronautical Quarterly*, 33(1):25–58, 1982.
- [13] Awatef Hamed, Keith Numbers, Awatef Hamed, and Keith Numbers. Inlet distortion considerations for high cycle fatigue in gas turbine engine. In *33rd Joint Propulsion Conference and Exhibit*, page 3364, 1997.
- [14] RG Hercock and DD Williams. Distortion-induced engine instability aerodynamic response. *AGARD, LS72-Paper*, 3, 1974.
- [15] HWM Hoeijmakers, W Vaatstra, and NG Verhaagen. Vortex flow over delta and double-delta wings. *Journal of aircraft*, 20(9):825–832, 1983.
- [16] Kevin M Hoopes. *A new method for generating swirl inlet distortion for jet engine research*. PhD thesis, Virginia Tech, 2013.
- [17] Adam Jirasek. Development and application of design strategy for design of vortex generator flow control in inlets. In *44th AIAA Aerospace Sciences Meeting and Exhibit*, page 1050, 2006.

- [18] Byung Joon Lee, Takayasu Kumano, and Meng-Sing Liou. Design exploration for vortex generators for boundary-layer-ingesting inlet. In *13th AIAA/ISSMO Multidisciplinary Analysis Optimization Conference*, page 9399, 2010.
- [19] KW Lotter and J Jörg. The effect of intake flow disturbances on apu compressor blade high cycle fatigue in the airbus a300. In *Proceedings of the 13th Congress of ICAS/AIAA. Seattle: ICAS-82*, volume 4, 1982.
- [20] NS Diaconis NACATN. Nacatn 2730. two-dimensional shear flow in a 90 elbow. jj kramer and jd stanitz. nacatn• 2736. matrix and relaxation solutions that determine subsonic through flow in an axial-flow gas turbine. chung-hua wu. nacatn 2750.
- [21] W Pazur and L Fottner. The influence of inlet swirl distortions on the performance of a jet propulsion two-stage axial compressor. 1991.
- [22] W Duncan Rannie and Frank E Marble. Unsteady flows in axial turbomachines. 1957.
- [23] M Rowe. Measurements and computations of flow in pipe bends. *Journal of Fluid Mechanics*, 43(4):771–783, 1970.
- [24] Norbert R Schmid, Dirk C Leinhos, and Leonhard Fottner. Steady performance measurements of a turbofan engine with inlet distortions containing co-and counterrotating swirl from an intake diffuser for hypersonic flight. *J. Turbomach.*, 123(2):379–385, 2001.
- [25] William Schneck, Anthony Ferrar, Justin Bailey, Kevin Hoopes, and Walter O’Brien. Improved prediction method for the design of high-resolution total pressure distortion screens. In *51st AIAA Aerospace Sciences Meeting including the New Horizons Forum and Aerospace Exposition*, page 1133, 2013.
- [26] Yogi Sheoran and Bruce Bouldin. A versatile design of a controlled swirl distortion generator for testing gas turbine engines. In *Turbo Expo: Power for Land, Sea, and Air*, volume 43116, pages 81–92, 2008.

- [27] Yogi Sheoran, Bruce Bouldin, and P Murali Krishnan. Advancements in the design of an adaptable swirl distortion generator for testing gas turbine engines. In *Turbo Expo: Power for Land, Sea, and Air*, volume 48821, pages 23–32, 2009.
- [28] Yogi Sheoran, Bruce Bouldin, and P Murali Krishnan. Compressor performance and operability in swirl distortion. 2012.
- [29] Guoxing Song, Jun Li, Mengxiao Tang, Wu Yun, and Luo Yanhao. Experimental simulation methodology and spatial transition of complex distortion fields in a s-shaped inlet. *Aerospace Science and Technology*, page 106855, 2021.
- [30] CP Stocks and NC Bissinger. The design and development of the tornado engine air intake. *AGARD Aerodyn. of Power Plant Installation 21 p(SEE N 82-13065 04-01)*, 1981.
- [31] JP Sullivan, SNB Murthy, R Davis, and S Hong. S-shaped duct flows. *Office of Naval Research Contract Number N-78-C-0710*, 1982.
- [32] Shu Sun, Hui-Jun Tan, and Chen-Xi Wang. Submerged inlet performance enhancement using a unique bump-shaped vortex generator. *Journal of Propulsion and Power*, 32(5):1275–1280, 2016.
- [33] Geoffrey Tanguy, David G MacManus, Pavlos Zachos, Daniel Gil-Prieto, and Eric Garnier. Passive flow control study in an s-duct using stereo particle image velocimetry. *AIAA Journal*, 55(6):1862–1877, 2017.
- [34] John C Vaccaro, Yossef Elimelech, Yi Chen, Onkar Sahni, Kenneth E Jansen, and Michael Amitay. Experimental and numerical investigation on the flow field within a compact inlet duct. *International journal of heat and fluid flow*, 44:478–488, 2013.
- [35] AD Vakili, JM Wu, MK Bhat, and P Liver. Compressible flow in a diffusing s-duct with flow separation. *Heat transfer and fluid flow in rotating machinery*, pages 201–211, 1987.
- [36] SR Wellborn, BA Reichert, and TH Okiishi. An experimental investigation of the flow in a diffusing s-duct. aiaa paper 92-3622 presented at the aiaa.

- SAE/ASME/ASEE 28th Joint Propulsion Conference, 1992.
- [37] Steven R Wellborn, Theodore H Okiishi, and Bruce A Reichert. A study of the compressible flow through a diffusing s-duct. 1993.
- [38] B Wendt and B Reichert. The modelling of symmetric airfoil vortex generators. In *34th Aerospace Sciences Meeting and Exhibit*, page 807, 1996.
- [39] Michael M Wojewodka, Craig White, Shahrokh Shahpar, and Konstantinos Kontis. A review of flow control techniques and optimisation in s-shaped ducts. *International Journal of Heat and Fluid Flow*, 74:223–235, 2018.
- [40] Pavlos K Zachos, David G MacManus, Daniel Gil Prieto, and Nicola Chiereghin. Flow distortion measurements in convoluted aeroengine intakes. *AIAA Journal*, 54(9):2819–2832, 2016.

Appendix A

Potential Flow

Initially it was planned to fit the velocity field obtained through simulations on the AIP section using the 2D potential flow of an arbitrary number of Lamb-Oseen vortices. The complex velocity $\mathbf{u} = u_x + ju_y$ induced by a vortex core z_0 with a circulation *gamma* and a radius a_0 is expressed according to the following relation:

$$\left\{ \begin{array}{ll} \bar{\mathbf{u}}_{\Gamma, a_0}(\mathbf{z} - \mathbf{z}_0) = u_x - ju_y = \frac{\Gamma}{2j\pi} \frac{1}{\mathbf{z} - \mathbf{z}_0} \left[1 - \exp\left(-\frac{|\mathbf{z} - \mathbf{z}_0|^2}{a_0^2}\right) \right] & \text{if } \mathbf{z} \neq \mathbf{z}_0 \\ = 0 & \text{if } \mathbf{z} = \mathbf{z}_0 \end{array} \right. \quad (\text{A.1})$$

The wall boundary condition is simulated by a complementary image vortex (with opposite circulation) with its core placed at $1/\bar{z}_0$, leading to:

$$\bar{\mathbf{u}} = u_x - ju_y = \frac{\Gamma}{2j\pi} \frac{1}{\mathbf{z} - \mathbf{z}_0} \left[1 - \exp\left(-\frac{|\mathbf{z} - \mathbf{z}_0|^2}{a_0^2}\right) \right] + \underbrace{\frac{-\Gamma}{2j\pi} \frac{1}{\mathbf{z} - 1/\bar{z}_0} \left[1 - \exp\left(-\frac{|\mathbf{z} - 1/\bar{z}_0|^2}{a_0^2}\right) \right]}_{\bar{u}^* \text{ image vortex}} \quad (\text{A.2})$$

Fitting the CFD solution with the potential flow allows us, for each velocity field in the AIP, to define the parameters that characterise the vortices, i.e. z_0 , γ and a_0 and this serves as a metric to compare the different solutions. Figure A.1 shows

the contour of the difference between the velocity field obtained with CFD and that obtained with potential flow. The Figure A.1 also shows the streamlines for both the potential flow (black) and the CFD solution (blue). Analyzing Figure A.1a The streamlines near the vortex core seem to fit those of the RANS solution quite well, but the further away from the vortex core we go, the more the discrepancies between the two solutions increase. Furthermore, looking at the contour, we can see that near the vortex core there is a region where the error is around 2.5 and 5 m/s which represents about 30 % of the velocity in that region. In addition, looking at Figures A.1b, A.1c and A.1d it can be seen that by complicating the shape of the vortex or simply by increasing the number of vortices it becomes more and more difficult to fit the RANS solution to the potential flow.

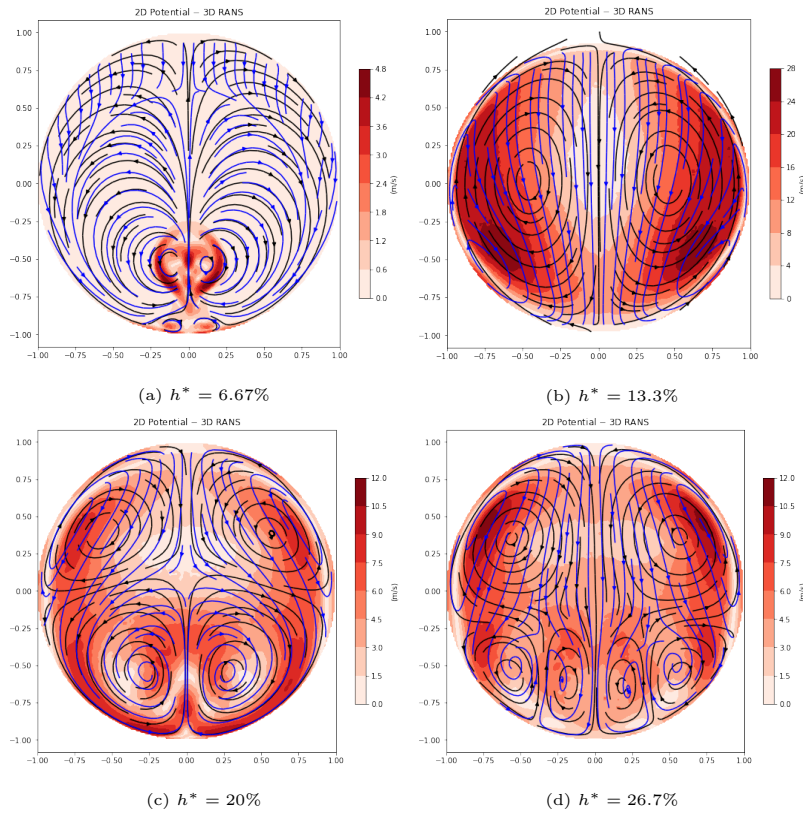


Figure A.1: Inlet-Y: swirl angle profile (a) and streamlines in the AIP (b).